Ore Geology Reviews 92 (2018) 1–18

Contents lists available at ScienceDirect

Ore Geology Reviews

journal homepage: www.elsevier.com/locate/oregeorev

Mineralogy, geochemistry and fluid inclusions of the Qinglong Sb-(Au) deposit, Youjiang basin (Guizhou, SW China)

Jun Chen[a], Rui-Dong Yang[a,*], Li-Juan Du[a,b], Lu-Lin Zheng[a], Jun-Bo Gao[a], Chun-Kit Lai[c,d], Huai-Rui Wei[a], Ming-Gang Yuan[e]

[a] College of Resources and Environmental Engineering, Guizhou University, Guiyang 550025, PR China
[b] State Key Laboratory of Ore Deposit Geochemistry, Institute of Geochemistry, Chinese Academy of Sciences, Guiyang 550002, PR China
[c] Faculty of Science, Universiti Brunei Darussalam, Gadong BE1410, Brunei Darussalam
[d] ARC Centre for Excellence in Ore Deposits (CODES), University of Tasmania, Hobart 7001, Australia
[e] Guizhou Qinglong Antimony Mining District, Qinglong County 561400, Guizhou Province, PR China

ARTICLE INFO

Keywords:
Qinglong Sb-(Au) deposit
Youjiang basin (Guizhou, SW China)
Stibnite
Fluid inclusions
Fluid evolution

ABSTRACT

The Qinglong deposit is a newly-characterized, large Sb-(Au) deposit in the Youjiang basin (Guizhou, SW China). Four mineralization stages are identified (i.e., pre-ore, early-ore, late-ore and post-ore) in this study based on crosscutting relationships. Our study shows that the Qinglong Sb mineralization (early-ore stage) was dominated by quartz-stibnite ± fluorite, whilst the Sb-Au mineralization (late-ore stage) comprises quartz-stibnite ± pyrite. Electron Probe Microanalysis (EPMA) indicates that the Au is present as Au^{1+} in the arsenian pyrite. Besides, our new fluid inclusion data from fluorite, stibnite and quartz show that the Sb-Au-rich hydrothermal fluids were derived from the mixing fluids consisting of H_2O, NaCl, hydrocarbon and minor CO_2. In the early-ore stage, the ore-forming fluids are characterized by medium to low temperatures (161–294 °C, mean: 220 °C), medium to low salinities (0.35–13.18 wt% NaCl equiv.), low pH, and the presence of hydrocarbons and CO_2. In comparison, the late-ore stage ore-forming fluids are featured by low temperatures (113–255 °C, mean: 175 °C), low salinities (0.18–6.30 wt% NaCl equiv.) and nearly neutral pH. The $\delta^{34}S_{\Sigma S}$ values (−2.8 to 2.3‰) of the ore-forming fluids suggest that the sulfur at Qinglong was dominantly magmatic-derived. From the early-ore to late-ore stage, the ore-forming fluid temperature and oxygen fugacity (fO_2) decrease but the pH increases (from acidic to neutral). Such physicochemical transition may have significantly decreased the Sb solubility from 10 s to 100 s of ppm to 0.001 ppm. Therefore, we propose that fluid mixing was the main process that substantially reduced the fluid temperature and oxygen fugacity, which effectively lowered the Sb solubility and led to abundant stibnite precipitation. The stibnite precipitation had likely decreased the H_2S concentrations of the ore-forming fluids, thereby destabilizing the $AuHS^0$ complexes in the fluids and caused local Au precipitation.

1. Introduction

The Youjiang basin (Guizhou, SW China) is a key constituent of a low-temperature metallogenic province in South China (Fig. 1), which contains a number of large Sb and Carlin-style Au deposits, such as the Qinglong Sb-(Au) deposit, and the Lannigou, Shuiyindong, Zimudang, Getang and Nibao Carlin-style Au deposits (Hu et al., 2002, 2007; Hu and Zhou, 2012; Huang et al., 2011) (Fig. 1). In particular, the Qinglong Sb-(Au) deposit (the largest Sb deposit in the basin) contains a proven and an inferred Sb resource of ca. 300,000 tonnes and 70,000 tonnes, respectively (Guizhou BGMR, unpublished). Previous studies have documented that the Sb mineralization at Qinglong (fluorite Sm-Nd age: ca. 142–148 Ma; Peng et al., 2003) was formed in similar age and tectonic setting (Wang et al., 2012; Hu and Zhou, 2012) to the Carlin-style Au deposits in the Youjiang basin (quartz Rb-Sr age: ca. 134–136 Ma; Su et al., 2009b), which suggests a possible genetic relationships between the two. Recent exploration at Qinglong also discovered extensive Au mineralization (0.1–9.9 g/t) (Guizhou BGMR, unpublished) hosted by the “Dachang layer”, a silicic alteration zone of volcaniclastic rocks and the Emeishan basalt (Yang et al., 2009). However, no detailed study has been carried out on this newly discovered and important Au mineralization at Qinglong, and the genetic relationships, if any, between the Sb-Au mineralization and the “Dachang layer” are yet to be determined. Another question is whether the Au mineralization at Qinglong is similar to the Carlin-style Au mineralization nearby, resolving which would require knowledge in the

* Corresponding author.
E-mail address: rdyang@gzu.edu.cn (R.-D. Yang).

https://doi.org/10.1016/j.oregeorev.2017.11.009
Received 16 May 2017; Received in revised form 28 October 2017; Accepted 8 November 2017
Available online 10 November 2017
0169-1368/

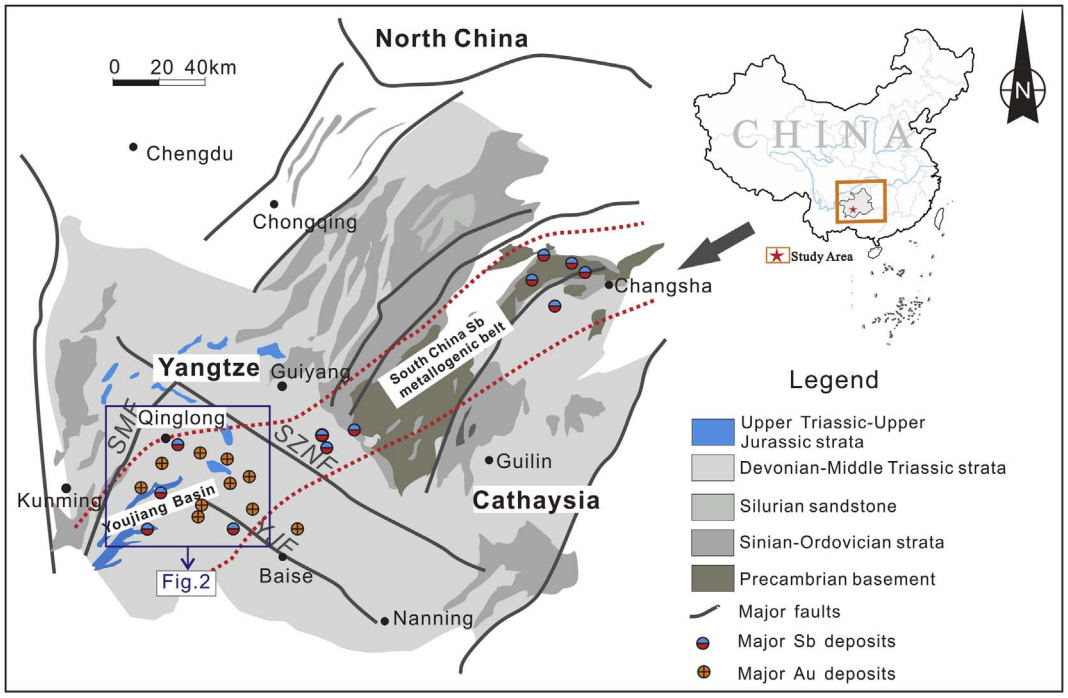

Fig. 1. Location map, showing the major gold and antimony deposits in the southwestern Yangtze Craton, China (modified after Hu et al., 2002). Abbreviations: SZNF = Shuicheng-Ziyun-Nandan Fault; SMF = Shizong-Mile Fault; YJF = Youjiang Fault.

precise mineralization age, ore-forming material source and evolution of the Qinglong deposit, building on previous research works on the Carlin-style Au deposits in the Youjiang basin (e.g., Hu et al., 2002; Hu and Zhou, 2012; Peters et al., 2007; Su et al., 2008, 2009a,b, 2012, 2017; Huang et al., 2011; Chen et al., 2015; Tan et al., 2015; Hou et al., 2016; Pi et al., 2017; Zhu et al., 2017).

Fluorite and quartz are the major gangue minerals at Qinglong, which provide an ideal ground for fluid inclusion (FI) studies. With the development of infrared microscopy temperature measurement technology, it is now also feasible to directly analyze the FIs in the ore minerals (e.g., stibnite, pyrite and chalcopyrite) to reveal the physico-chemical conditions of the ore-forming fluids (Buchholz et al., 2007; Ge et al., 2011; Ni et al., 2015; Sun et al., 2014; Zhu and Peng, 2015). Previous FI studies on the Qinglong deposit are largely inadequate and only limited to the transparent gangue minerals (Chen, 1992; Ye, 1996; Ye et al., 1997; Wang et al., 2013; Xiong et al., 2013; Liu et al., 2016). Su et al. (2015) first conducted infrared microscopic temperature analysis on the FIs from the Qinglong drusy stibnite, and suggested that the hydrothermal fluids that formed the stibnite and fluorite may have had different origins, but the fluid evolutionary process is still unclear. In this paper, we describe the geological features of the Qinglong deposit, summarize the mineralization information, and interpret the fluid inclusion and sulfur isotope data to reveal the sources and evolution of the ore-forming fluids, as well as the genesis of the Qinglong Sb-(Au) deposit.

2. Geological background

2.1. Regional geology

The Youjiang basin is located in the southwestern margin of the Yangtze Block. The basin is bounded by the Shuicheng–Ziyun–Nandan fault in the northeast and by the Shizong–Mile fault in the west (Fig. 2). Previous studies suggested that the Youjiang basin had experienced multi-stage deformation from the Late Devonian (ca. 364 Ma) to the Early Cretaceous (ca. 142 Ma). This includes the folding-thrusting and uplift during the late Caledonian Orogeny, the Devonian–Triassic extensional tectonics, the late Indosinian foreland fold-thrust tectonics, and the Yanshanian–Himalayan uplift and denudation (Guizhou BGMR, 1987). These tectonic events, especially the Yanshanian one, have formed the complex structures and widespread low-temperature Sb-Au-As-Hg mineralization in the basin (Fig. 2; Li and Peters, 1998; Peng et al., 2003; Peters et al., 2007; Su et al., 2009b, 2012; Huang et al., 2011; Hu and Zhou, 2012).

Magmatism in the Youjiang basin is represented by the Late Permian dolerite intrusions (zircon U-Pb age: ~259 Ma; Zhang and Xiao, 2014), quartz porphyry dykes (zircon U-Pb age: 140–130 Ma; Zhu et al., 2016) and lamprophyre dykes (zircon U-Pb age: 88–85 Ma; Liu et al., 2010) in the southeastern and northern parts of the basin, respectively (Fig. 2). A wide range of ages (various dating methods: 275–46 Ma) have been reported for the Carlin-style Au mineralization in the Youjiang basin (e.g., Hu et al., 1995, 2002; Su et al., 2009b; Chen et al., 2015; Pi et al., 2017), but these ages mainly cluster around Late Triassic (235–200 Ma; Chen et al., 2009, 2015; Pi et al., 2017) and Late Jurassic to Early Cretaceous (148–134 Ma; Li et al., 1995; Liu et al., 2006; Su et al., 2009b). The Late Jurassic to Early Cretaceous magmatism is broadly coeval with the published ages of the regional Sb mineralization (fluorite Sm-Nd isochron age: 148–142 Ma; Peng et al., 2003). It is noteworthy that felsic dykes are present in some Carlin-style Au ore fields, and their ages (zircon U-Pb age: 140–130 Ma) are similar to the regional Au-Sb mineralization (Zhu et al., 2016). In addition, aeromagnetic surveys reveal deep-lying plutons in the Youjiang basin (Wang et al., 2009, 2015), which leads to proposals that these felsic dykes and the Au-Sb mineralization are genetically linked (Guo, 2000; Huang and Cui, 2001; Ma et al., 2013; Li et al., 2014; Chen et al., 2016; Zhu et al., 2016).

2.2. Ore deposit geology

The Qinglong deposit contains eight ore blocks (i.e., Dachang, Shuijingwan, Dishuiyan, Gulu, Houpo, Xishe, Sanwangping and Heishanjing), and Au and fluorite deposits are discovered near Qinglong (Fig. 3). The Qinglong deposit is characterized by a dome structure with complex faulting. These faults are either NE-striking

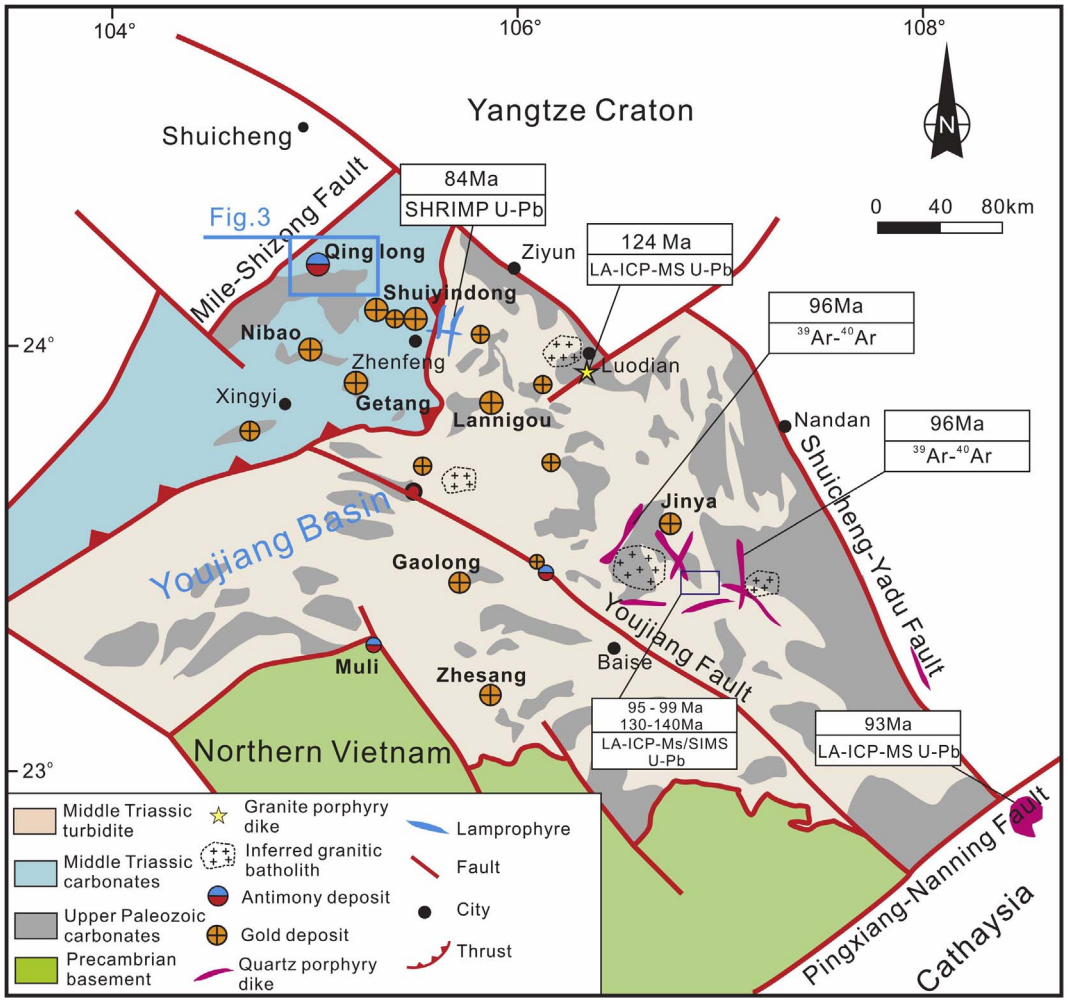

Fig. 2. Simplified geologic map, showing the distribution of tectonic units, intrusive rocks and Au-Sb deposits in the Youjiang basin, SW China (modified from Hou et al., 2016; Zhu et al., 2017; Su et al., 2017). Ages for intrusive rocks are summarized from Wang et al. (2004), Li et al. (2008), Mao et al. (2013), Zhu et al. (2016, 2017) and Su et al. (2017).

(e.g., the Huayujing, Yezhutang and Qingshanzhen faults) or EW-striking (e.g., the Angu fault) (Fig. 3). Silicic and fluorite alterations are present along the fault zones, indicating that these faults were probably fluid pathways during the regional Sb-Au mineralization. All the Sb and Au deposits are hosted in the dome structure.

Rocks exposed at Qinglong are dominated by the Middle Permian Maokou Formation, the "Dachang layer", the Upper Permian Emeishan flood basalt and the Longtan Formation (Figs. 3 and 4). The Maokou Formation comprises shallow-marine platform carbonates (Fig. 4). The Dachang layer lies above the Maokou Formation and is divided into the lower, middle and upper units (Fig. 4). The lower unit consists of detrital quartz, argillite and silicified limestone. The middle unit is dominated by brecciated basalt, tuff and silicified limestone with relatively high porosity, and is the main ore host of the quartz-stibnite ± fluorite (Qtz-Stb ± Fl)-type orebodies (Fig. 4). The upper unit is composed of tuff and carbonaceous mudstone, which hosts the quartz-stibnite ± pyrite (Qtz-Stb ± Py)-type orebodies and the Au mineralization (Fig. 4). The Emeishan flood basalt is tholeiitic (Liao, 2013; Chen et al., 2014). The Longtan Formation comprises interbedded sandstone and shale. The Dachang layer is the main ore host of the Qinglong deposit (Fig. 4).

Two types of orebodies are recognized in this study: The Qtz-Stb ± Fl-type orebodies account for ca. 80% of the Qinglong Sb reserves, with an average grade of 3.94% Sb (Guizhou BGMR, unpublished). These orebodies are generally lensoidal, and are hosted in the middle unit of the Dachang layer (Figs. 4 and 7A). Individual orebodies range from 50 m to 610 m long and 40 m to 120 m wide, dipping at 3° to 8° to the northwest. Alteration associated with the Sb mineralization includes silicic and kaolinite.

The Qtz-Stb ± Py-type stratiform and vein orebodies (Fig. 5C–E) are hosted in the middle and upper units of the Dachang layer, and commonly crosscut the older Qtz-Stb ± Fl-type orebodies (Figs. 5A–E; 6B). Although this orebody type accounts for only ~10% of the Sb reserves at Qinglong, it hosts the majority of the Au mineralization. The mineralization-related alterations include mainly pyrite, silicic and illite.

Based on field crosscutting relationships and mineral paragenesis, four mineralization stages (i.e., pre-ore, early-ore, late-ore and post-ore) have been identified at Qinglong (Fig. 9). The pre-ore stage (Stage I) is characterized by detrital quartz, marcasite, organic matter and fine-grained globular pyrite (Py-I) (Fig. 6A). The early-ore stage (Stage IIa) is the main Sb mineralization stage, and contains mainly quartz (Qtz-IIa), fluorite (Fl-IIa), stibnite (Stb-IIa) (Figs. 6D–G; 7A–D) and kaolinite (Fig. 19). Commonly, the quartz and fluorite are crosscut (Fig. 7A and C) or included (Fig. 7D) by the stibnite, indicating that the latter was formed slightly later. The Qtz-Stb ± Fl-type orebodies are formed in this stage.

The late-ore stage (Stage IIb) is the main Sb-Au mineralization stage, and formed the Qtz-Stb ± Py-type stratiform/vein orebodies. Major minerals include veined quartz (Qtz-IIb; Figs. 6C, 8A–D), fine-grained stibnite (Stb-IIb; Fig. 6H-I), arsenian pyrite (Py-IIb; Fig. 10A–E) and illite (Fig. 10D), together with minor chalcopyrite (Fig. 10F), Fe-Sb

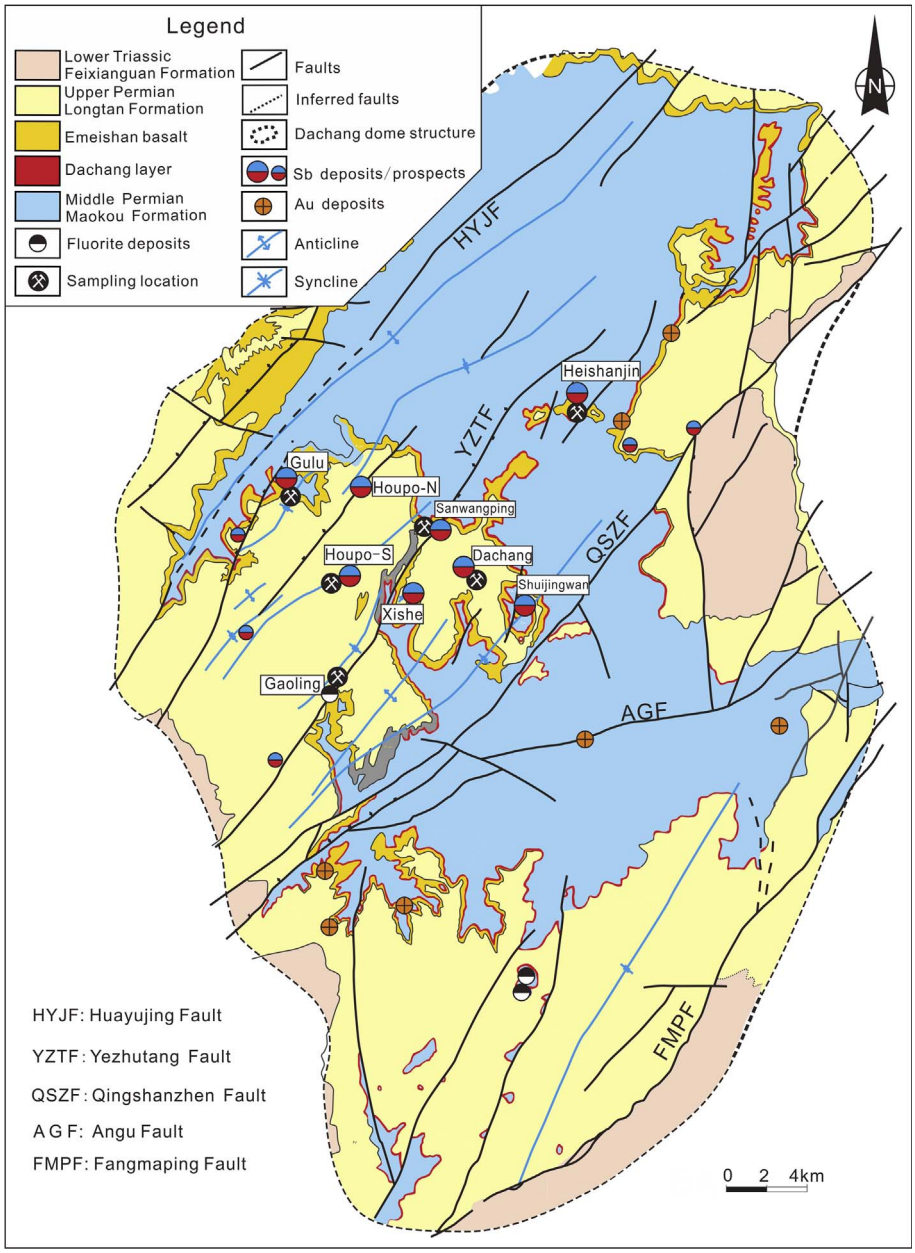

Fig. 3. Geologic map of the Qinglong deposit (modified after the Guizhou BGMR, unpublished).

tetrahedrite (Fig. 10B) and arsenopyrite. It is noteworthy that Py-IIb generally occurs as rims of Py-I. The post-ore stage contains mainly secondary Sb and Cu minerals, such as valentinite and malachite. Together with limonite, these supergene minerals occur mainly near the surface at Qinglong.

3. Samples and analytical methods

Ore samples were collected from field outcrops and underground tunnels of the different Qinglong ore blocks (Fig. 3). All the Au ore samples were collected from No. 1 adit of the Dachang ore block (Fig. 3). Petrographic observations were conducted on 18 polished hand specimens and 45 polished thin sections. Reflected and transmitted light microscopy, scanning electron microscopy (SEM), and electron probe microanalysis (EPMA) were conducted to examine the mineral paragenesis.

All of the above-mentioned analyses were performed at the State Key Laboratory of Ore Deposit Geochemistry, Institute of Geochemistry, Chinese Academy of Sciences (CAS). The Au fire assay and geochemical mapping were performed, respectively, at the ALS Chemex (Guangzhou) and the Institute of Geology and Geophysics, CAS. JSM-7800F SEM was used to identify minerals and provide semi-quantitative geochemical measurements. EPMA were conducted using a Shimadzu-1600 electron microprobe equipped with five wavelength dispersive spectrometers (WDS). Operating conditions included a 25 kV accelerating voltage, 10 nA beam current (10-s measurement time) and 10 μm spot size. Minimum detection limits for all the analyzed elements are around 200 ppm. Trace element (e.g., Au) distributions in the zoned pyrite are determined using a Cameca NanoSIMS 50L (Yang et al., 2015).

Microthermometric measurements of the stibnite inclusions were performed using a Linkam THMSG600 heating-freezing stage, which was attached to an Olympus BX51 infrared microscope connected to a ROLERA-XR infrared digital camera. Observation and microthermometric measurements for the fluid inclusions in the quartz and fluorite were performed using the conventional microthermometric measurement method. The estimated temperature measurement accuracy was ± 0.1 °C. The warming rate was ≤15 °C/min, and the warming rate

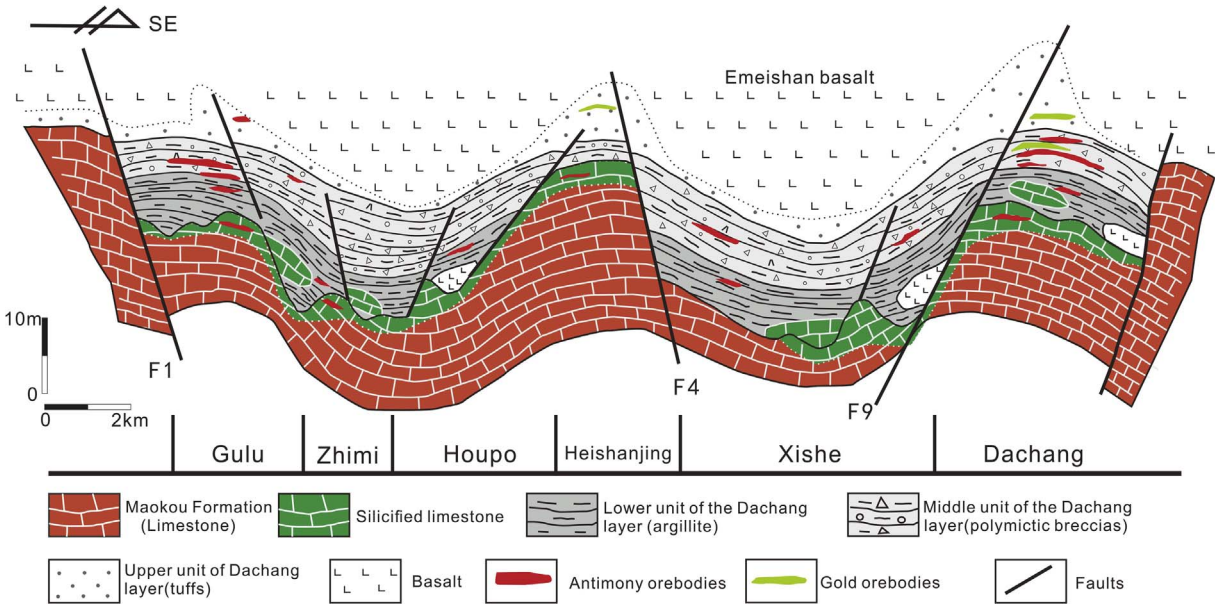

Fig. 4. Geologic cross section of the Qinglong deposit, showing the spatial relationship between the major orebodies and strata (modified from Guizhou BGMR, unpublished).

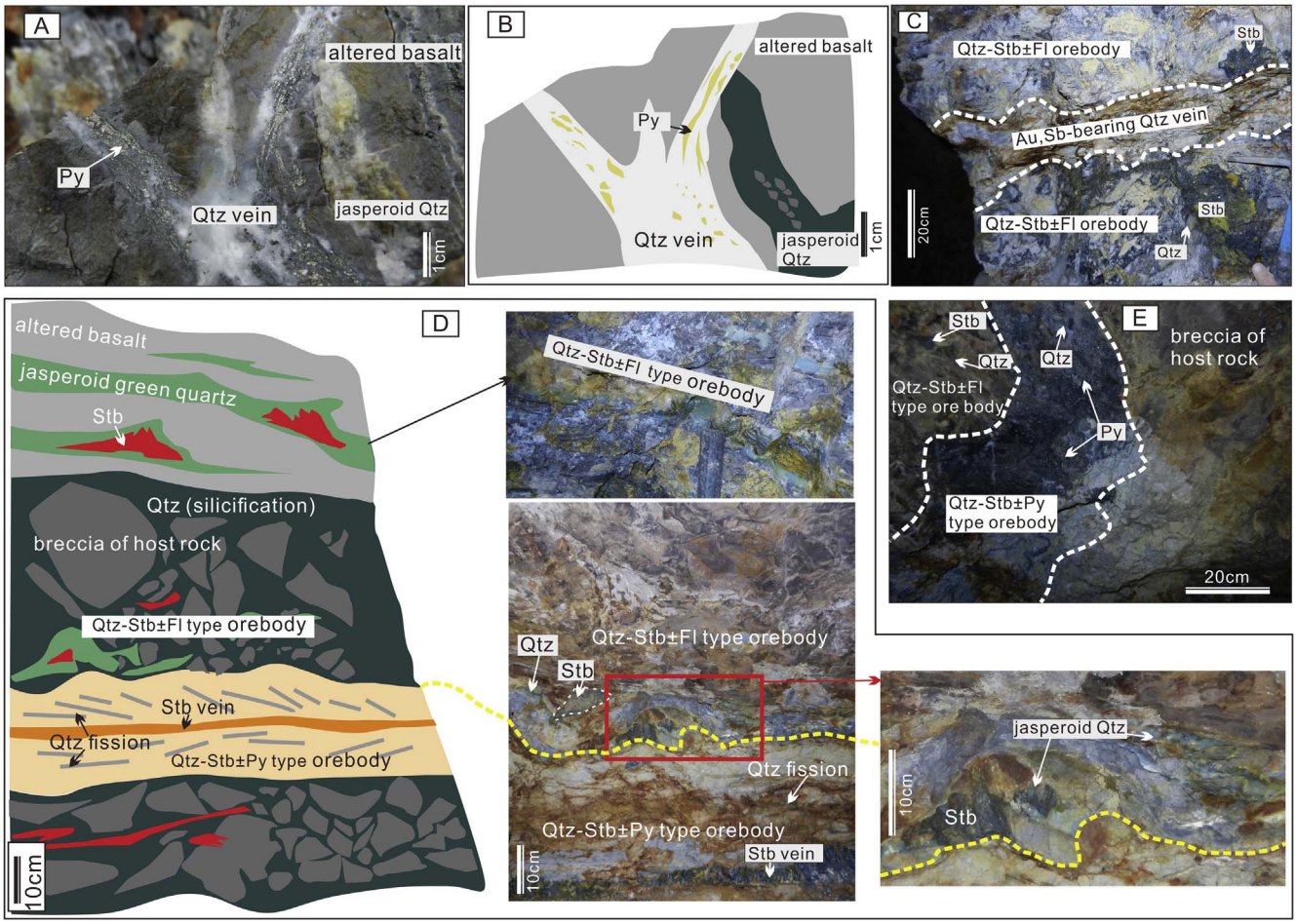

Fig. 5. Field photo and sketches, showing that the Qtz-Stb ± Fl-type orebodies formed before the Qtz-Stb ± Py-type orebodies. (A, B) Pyrite-bearing quartz vein crosscut altered basalt and jasperoid quartz. (C) Sb-bearing quartz vein crosscut the Qtz-Stb ± Fl-type orebodies; (D) Qtz-Stb ± Fl-type orebodies cut by Qtz-Stb ± Py-type orebodies, note that the former occur as lenses within the brecciated host rock. (E) Vein-like Qtz-Stb ± Py-type orebodies crosscut Qtz-Stb ± Fl-type orebodies. Abbreviations: Py = pyrite; Qtz = quartz; Stb = stibnite; Fl = fluorite.

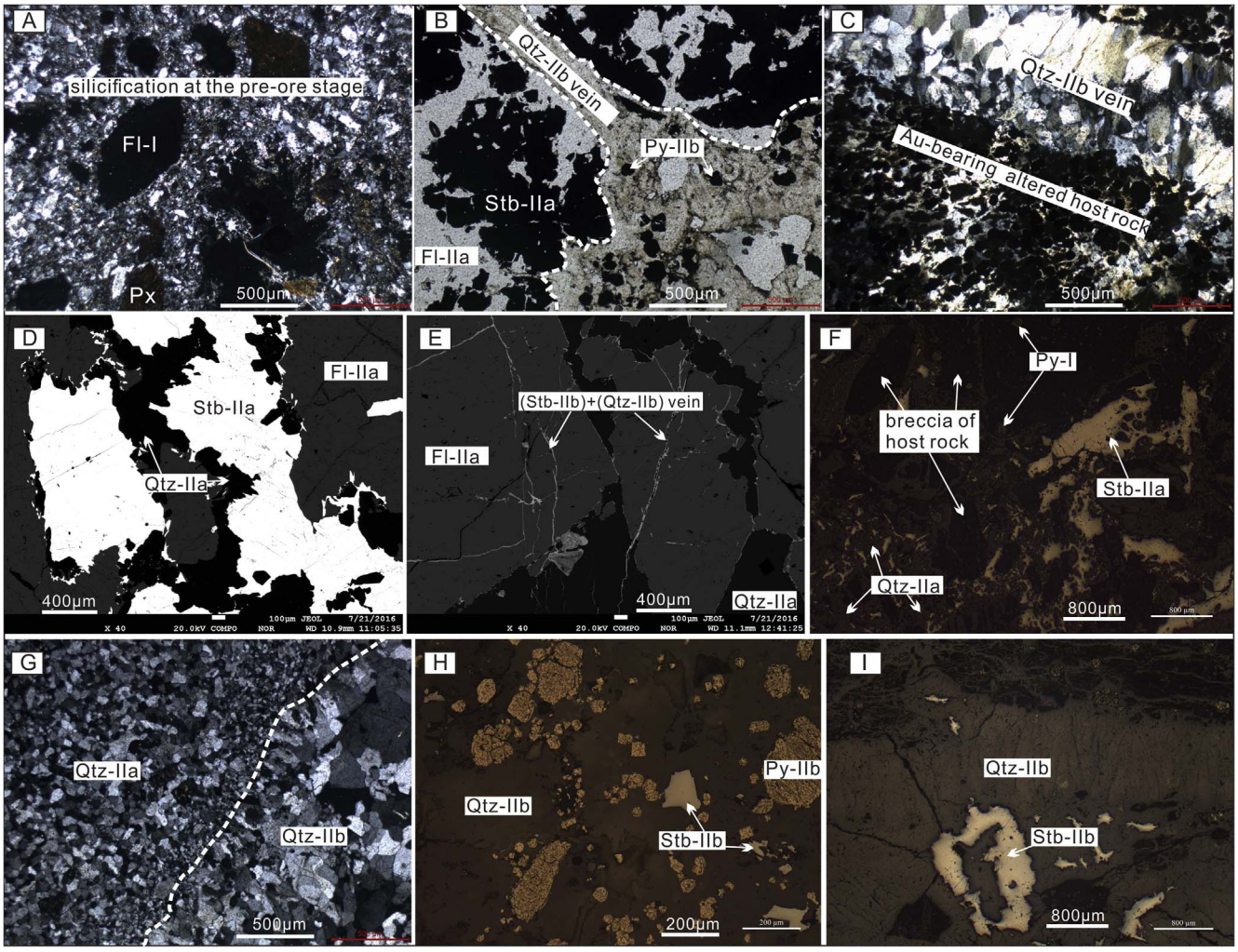

Fig. 6. Photomicrographs of minerals and their relationships in the Qinglong deposit. (A) Embayed-textured fluorite in silicified volcaniclastic rocks during diagenesis stage. (B) Early-stage stibnite and fluorite assemblage cut by late stage pyrite-bearing quartz veins. (C) Late-stage quartz vein fills in the pyritized host rock. (D) Euhedral-subhedral quartz and stibnite fills in early-stage fluorite. (E) Quartz + stibnite veinlets crosscut early-stage quartz + fluorite assemblage. (F) Early-stage stibnite in host rock breccia/fragments. (G) Late-stage subhedral quartz crosscuts fine-grained quartz. (H-I) Stibnite and/or pyrite distributed in late-stage quartz veins. Figures A, B, C and G were taken under transmitted light, figures F, H and I under reflected light, and figures D and E are backscattered electron (BSE) image. Abbreviations: Py = pyrite; Qtz = quartz; Stb = stibnite; Fl = fluorite.

was from 0.1 to 1 °C/min near the phase transition point. To minimize the effects of infrared light heat on the homogenization and freezing point temperatures of the fluid inclusions, we set the infrared light intensity to as low as possible during the course of the experiment (Ge et al., 2011). Additionally, in the freezing experiment of the medium- and low-salinity inclusions, we carried out uniform heating at first and freezing next to prevent the leakage of inclusion due to freezing expansion (Su et al., 2015).

Vapor and solid compositions of individual fluid inclusions in the quartz and fluorite were measured by the RenishawInVia Reflex laser Raman microspectroscopy. An Ar^+ ion laser operating at 20 mW was used to produce an excitation wavelength of 514 nm line. The scanning range of spectra was set between 140 and 4000 cm^{-1} with an accumulation time of 60 s for each scan.

Stibnite and pyrite were crushed to < 75 μm using an agate mortar for the sulfur isotope analysis. The samples were reacted with heated CuO to produce sulfur dioxide, and their $\delta^{34}S$ values were measured by a Thermo Finnigan MAT-253 mass spectrometer. The results are expressed as $\delta^{34}S$ relative to the Vienna Canyon Diablo Troilite (V-CDT). The analytical precision was ± 0.1‰. The fluid densities were calculated using the inclusion parameter calculation software Fincor 2 (Brown and Lamb, 1989).

4. Results

4.1. Mineral chemistry

EPMA results show consistent concentrations of S (28.12–28.37 wt %) and Sb (70.53–71.22 wt%) in Stb-IIa (Table 1), similar to the theoretical composition of stibnite (S: 28.62 wt%; Sb: 71.38 wt%) (Zhu, 2014). Stb-IIa also contains a minor amount of As (0.6–0.95 wt%). Elements such as Fe, Co, Ni and Zn are all below the detection limit. The Py-I core of the zoned pyrite contains minor As (< 1 wt%) and trace Sb, and Au is below the detection limit. Comparatively, the Py-IIb rim contains higher As (1.50–5.05 wt%), Au (200–1020 ppm) and trace Sb and Zn (Table 1). Stb-IIb consists of S (26.51–27.83 wt%), Sb (68.92–71.33 wt%) and minor Cu, showing a lower S content than the theoretical stibnite composition. Arsenic content in Stb-IIb (1.90–3.01 wt%).

Geochemical maps of representative zoned pyrite grains show a weakly positive ^{197}Au vs. ^{75}As correlation. The negative ^{34}S vs. ^{75}As correlation (Fig. 11) indicates the substitution of As for S in the pyrite lattice, and that gold is present in the As-rich part of the zoned pyrite (Reich et al., 2005; Deditius et al., 2008; Su et al., 2012).

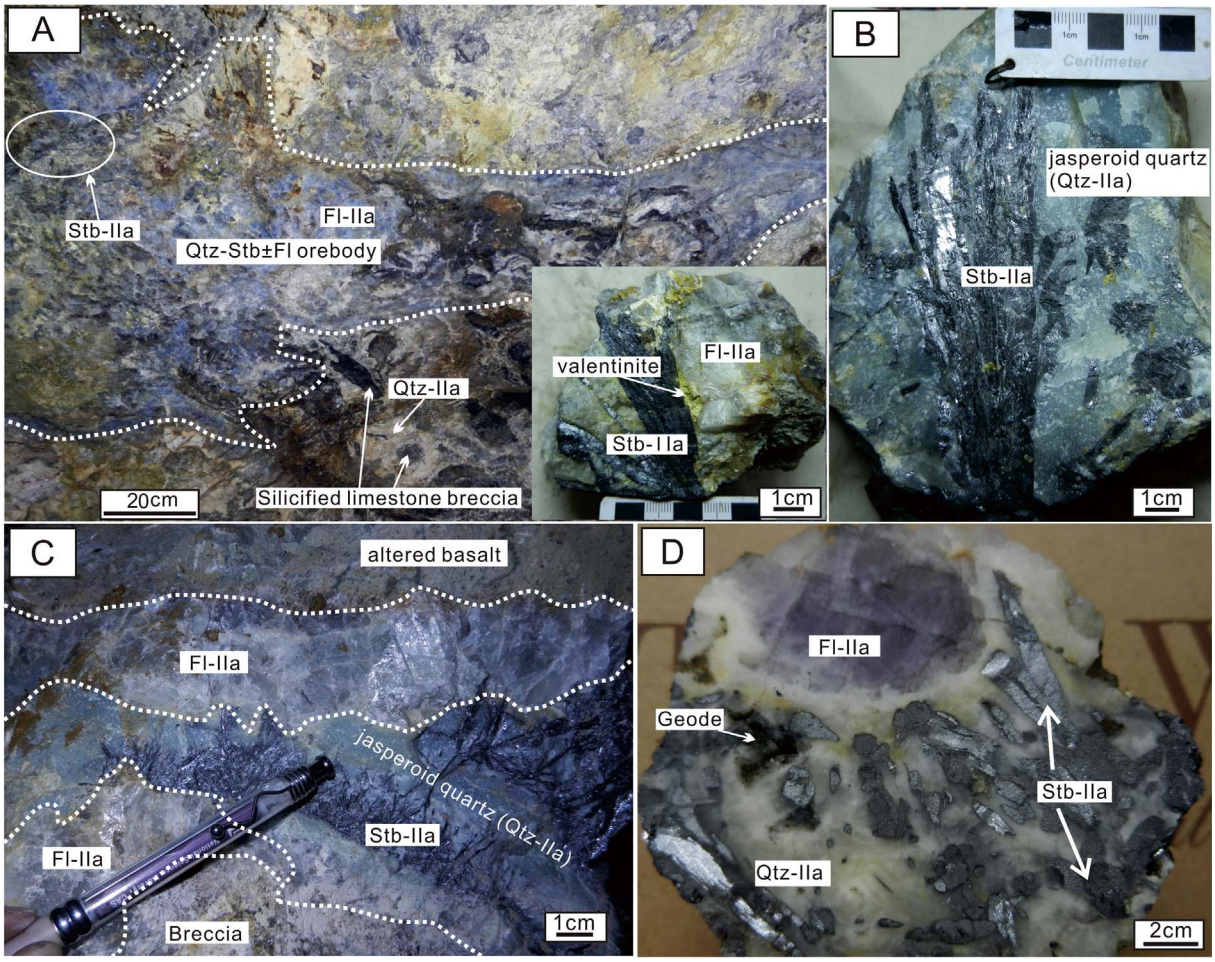

Fig. 7. Textural features and mineral paragenesis of the early-ore stage (IIa) Qtz-Stb ± Fl-type orebodies at Qinglong. (A) Lensoidal ore body within the middle unit of the Dachang layer, showing extensive fluorite, quartz and radiated stibnite (bottom right). (B-C) Stibnite in green jasperoid quartz. (D) Purple fluorite included by drusy stibnite and white jasperoid quartz. Abbreviations: Py = pyrite; Qtz = quartz; Stb = stibnite; Fl = fluorite. (For interpretation of the references to colour in this figure legend, the reader is referred to the web version of this article.)

4.2. Fluid inclusions petrography

Representative samples of Stb-IIa, Qtz-IIa and Fl-IIa of the early-ore stage (Fig. 12A) and Stb-IIb of the late-ore stage were selected for the fluids inclusion analysis. Primary, secondary and pseudo-secondary inclusions were selected based on the criteria proposed by Roedder (1984) and Lu et al. (2004). Microthermometric measurements in this study were performed on those inclusions considered as primary or pseudo-secondary. At Qinglong, five FI types were recognized based on the nature of phase relationships at room temperature and the phase transitions during the cooling and heating runs.

Type-I FIs are two-phase, liquid-rich aqueous inclusions with 5–30 vol% of a vapor bubble at room temperature. These inclusions range from 5 to 30 μm in diameter (except for those in stibnite, which are > 40 μm) (Fig. 12D–E), and can be classified into two sub-types based on their shapes: Type-Ia inclusions are negative crystal, cubic or elliptical (Fig. 12D–F, H–I), and generally occur in Stb-IIa (Fig. 12D-F). Type-Ib inclusions are irregularly-shaped (Fig. 12B and G), and occur in Fl-IIa (Fig. 12B) and/or Qtz-IIa (Fig. 12G).

Type-II FIs are single-phase aqueous inclusions. They are small in Qtz-IIa (3–6 μm) but large in Stb-IIb (15–25 μm) (Fig. 12D). These inclusions have generally negative crystal shape (Fig. 12B).

Type-III FIs are two-phase, vapor-rich aqueous inclusions with > 60 vol% of vapor bubble at room temperature (Fig. 12C, D, H). They are mainly 10–20 μm in diameter and have regular shape. Type-III FIs generally homogenized to vapor phase during heating. These inclusions occur together with Type-Ib, V and VI inclusions in Fl-IIa with a distinct dark vapor bubble (Fig. 12C), and coexist with Type-Ia and Type-II inclusions in Stb-IIb with a light-colored vapor bubble (Fig. 12H).

Type-IV FIs are single-phase, pure-gas inclusions. These inclusions only occur with Type-VI FIs in Fl-IIa (Fig. 12C).

Type-V FIs are organic matter-rich, and contain a black vapor phase and reddish-brown liquid phase. These inclusions mainly occur in Fl-IIa (Fig. 12C).

4.3. Microthermometric results

The FIs microthermometric results are listed in Table 2. Although Type-II, IV and V inclusions occur in Fl-IIa, Qtz-IIa and Stb-IIb, it was difficult to observe either ice-melting or homogenization temperatures in these inclusions.

4.3.1. Early-ore stage (Stage IIa)

4.3.1.1. Fluorite (Fl-IIa). Type-Ib inclusions in Fl-IIa have $T_{m\text{-}ice}$ (final melting temperature of ice) ranging from −1.8 to −0.6 °C (mean: −0.8 °C, n = 16), with corresponding salinities varying from 1.06 to 3.06 (mostly 1 to 2) wt% NaCl equiv. (mean: 1.48 wt% NaCl equiv., n = 16) (Fig. 13B). However, the homogenization temperatures (172–344 °C, mean: 262 °C, n = 26) of Type-Ib Fls are distinctly higher than those of Type-Ia FIs (Fig. 13A). The densities of Type-Ib Fls are of 0.715–0.911 g/cm^3 (mean: 0.814 g/cm^3, n = 19).

Type-III inclusions in Fl-IIa have homogenization temperatures of

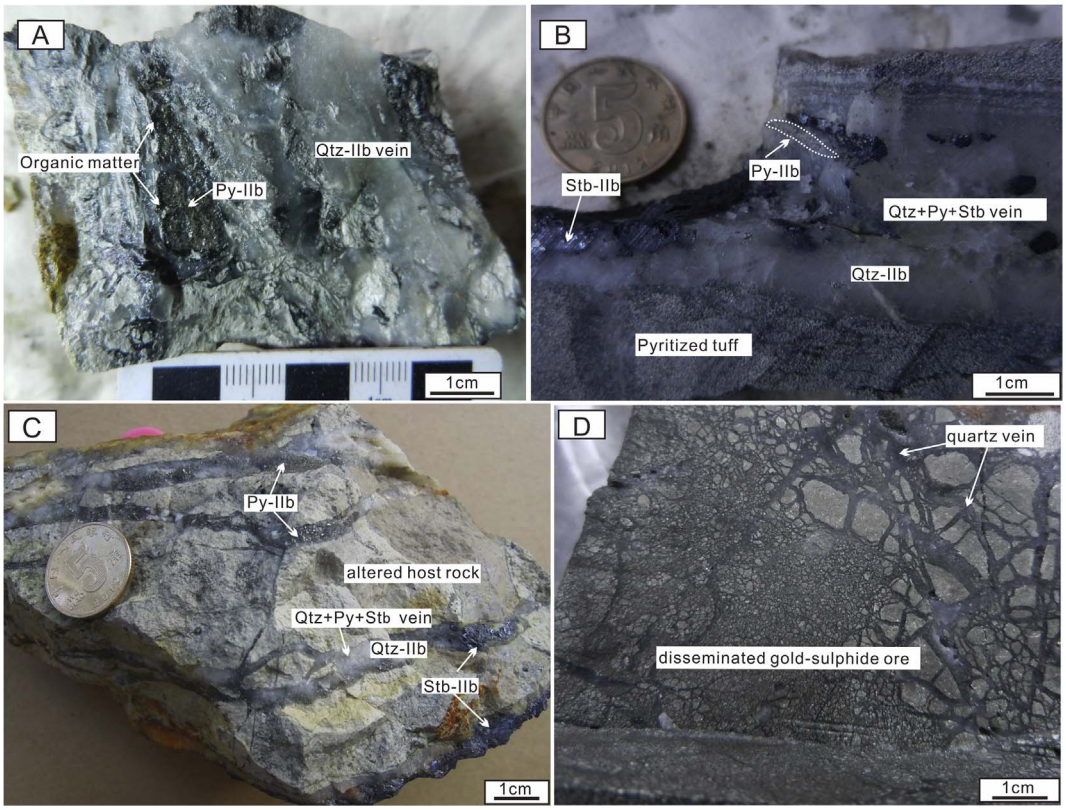

Fig. 8. Textural features and mineral paragenesis of the late-ore stage (IIb) Qtz-Stb ± Py-type orebodies at Qinglong. (A) Disseminated pyrite and veined quartz in the illite-altered host rock; (B) Pyrite-stibnite-quartz vein filled in pyritized tuff or argillic-altered basalt. (C) Bedding-parallel banded stibnite-quartz vein in altered host rock; (D) Disseminated Qtz-Stb ± Py type ore crosscut by quartz veinlets. Abbreviations: Py = pyrite; Qtz = quartz; Stb = stibnite; Fl = fluorite.

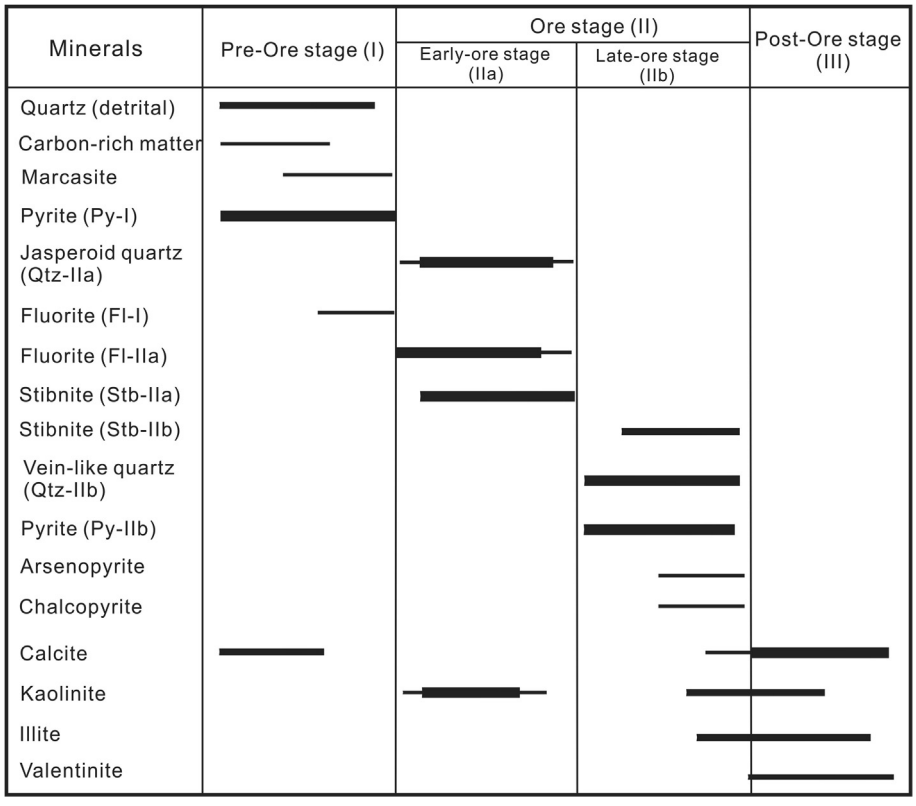

Fig. 9. Mineral paragenesis of the Qinglong deposit.

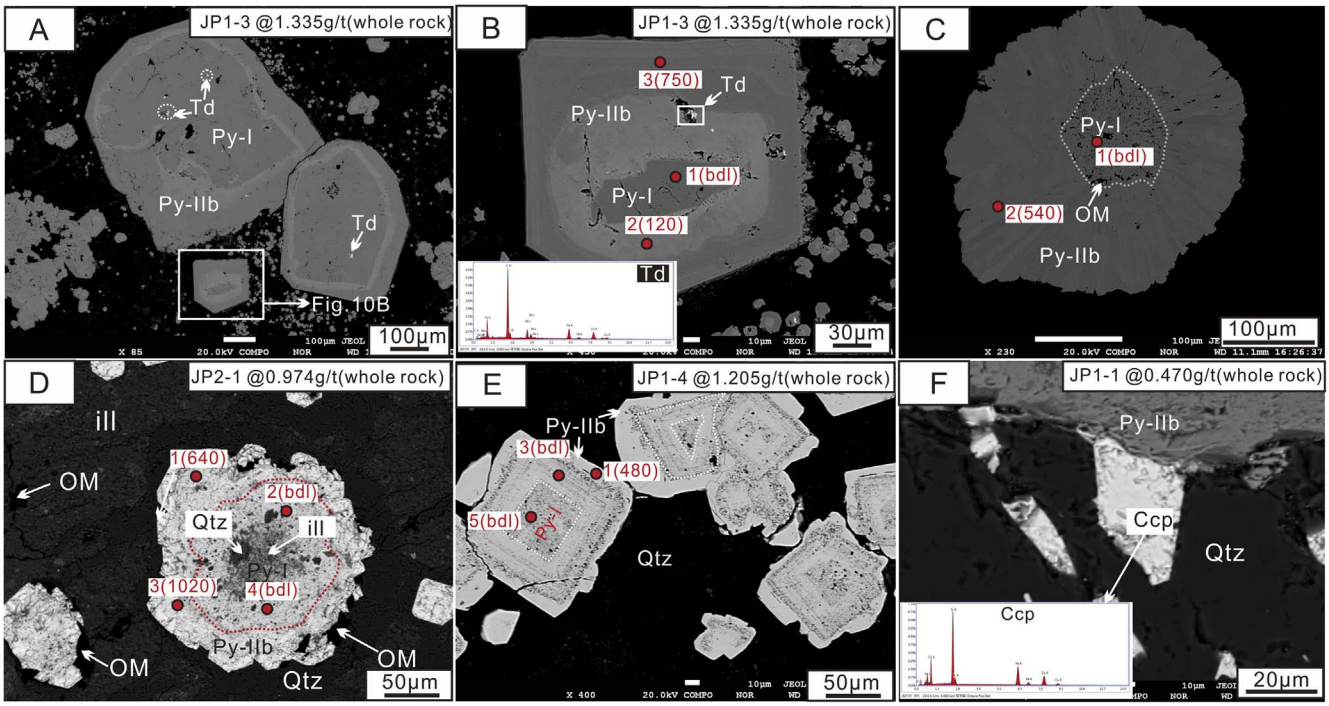

Fig. 10. Backscattered electron (BSE) images and gold concentration of the late-ore stage gold-bearing pyrite at Qinglong. (A-B) Zoned textured pyrite with Pyrite-I core (Au barren) and arsenian pyrite (Py-IIb) rim (Au: 200 ~ 750 ppm), which contains minor Fe-Sb tetrahedrite (Td). (C) BSE image of pyrite-I framboids and organic matter included by Py-IIb nodules. (D-E) Core-rim textured consists of cores of Py-I with metasomatic relict texture. (F) Chalcopyrite (Ccp) coexists with pyrite (Py-IIb) in quartz vein. Solid red dots represent EPMA analysis spots. Spot number and content (ppm) are also labeled. (For interpretation of the references to colour in this figure legend, the reader is referred to the web version of this article.)

Table 1
Representative EPMA data of the pyrite and stibnite from the Qinglong deposit (wt%).

Sample (Au grade)	Mineral	Point position	S	Fe	As	Au	Se	Ni	Co	Sb	Te	Zn	Total
JP1-3	Zoned	Core	53.88	45.48	0.53	0.02	bdl	bdl	bdl	bdl	bdl	0.01	99.95
(1.335 ppm)	pyrite		53.51	45.58	0.61	bdl	bdl	bdl	bdl	bdl	bdl	0.01	99.71
		As-pyrite overgrowth rim	51.71	44.42	3.27	0.07	bdl	bdl	bdl	bdl	bdl	bdl	99.47
			53.33	46.51	0.56	0.06	0.02	bdl	bdl	bdl	0.02	bdl	100.51
JP1-4	Zoned	As-pyrite overgrowth rim	52.08	45.23	2.21	0.03	bdl	bdl	bdl	0.03	0.06	bdl	99.65
(1.205 ppm)	pyrite		52.36	44.97	2.86	0.05	bdl	bdl	bdl	0.05	bdl	bdl	100.29
			52.13	45.76	3.38	0.04	bdl	bdl	bdl	bdl	bdl	bdl	101.35
			51.71	44.71	3.85	0.04	bdl	0.05	bdl	0.03	0.04	0.02	100.48
			50.70	44.76	5.02	0.05	bdl	bdl	bdl	0.07	bdl	0.05	100.63
		Core	53.61	45.69	1.77	0.02	bdl	bdl	bdl	bdl	0.02	bdl	101.12
			52.42	45.74	2.84	bdl	bdl	bdl	bdl	0.03	bdl	bdl	101.04
			51.72	45.89	2.49	bdl	0.02	bdl	bdl	0.05	bdl	bdl	100.17
			52.96	45.58	1.73	bdl	bdl	bdl	bdl	0.04	bdl	bdl	100.32
JP2-1	Zone pyrite	As-pyrite overgrowth rim	52.61	45.29	1.26	bdl	0.02	0.03	bdl	0.06	bdl	0.03	99.29
(0.974 ppm)			51.84	45.44	2.26	0.10	bdl	bdl	bdl	bdl	bdl	bdl	99.66
		Core	53.31	46.49	0.52	bdl	bdl	bdl	bdl	bdl	0.03	0.06	100.41
			53.42	45.88	0.64	0.06	0.02	bdl	bdl	bdl	bdl	bdl	100.03
JP1-1	Zoned	Core	53.74	46.57	0.64	0.04	bdl	bdl	bdl	bdl	bdl	bdl	101.00
(0.470 ppm)	pyrite		53.82	46.93	0.58	bdl	bdl	bdl	bdl	bdl	bdl	bdl	101.34
		As-pyrite overgrowth rim	50.10	45.31	4.45	0.05	bdl	bdl	bdl	bdl	bdl	bdl	99.93
			52.28	46.72	1.53	bdl	bdl	bdl	bdl	bdl	0.02	0.03	100.58
ST-2	Cubic pyrite in Qtz vein	Random spot	53.44	45.74	0.48	0.08	bdl	0.02	bdl	bdl	0.02	0.03	99.82
			53.42	45.26	0.54	0.06	bdl	bdl	bdl	bdl	bdl	bdl	99.30
			53.27	45.95	0.49	0.05	bdl	bdl	bdl	bdl	bdl	bdl	99.78
Sample	Mineral	Stage	S	Fe	Sb	As	Au	Cu	Zn	Ag	Pb		Total
DJ-5	Stibnite	Early-ore stage	28.37	bdl	71.22	0.95	bdl	bdl	bdl	bdl	bdl		100.56
		(Random spot)	28.12	bdl	70.53	0.63	bdl	bdl	bdl	bdl	bdl		99.29
			28.30	bdl	70.79	0.60	bdl	bdl	bdl	bdl	bdl		99.72
DJ2-3	Stibnite	Late-ore stage (Random spot)	26.51	bdl	71.33	2.36	bdl	0.05	bdl	bdl	bdl		100.24
			27.83	bdl	68.92	2.79	bdl	bdl	bdl	bdl	bdl		99.54
			27.22	bdl	70.39	1.90	bdl	0.04	bdl	bdl	bdl		99.55
			26.59	bdl	70.90	3.01	bdl	0.08	bdl	bdl	bdl		100.57

Bdl = below the detection limit (200 ppm).

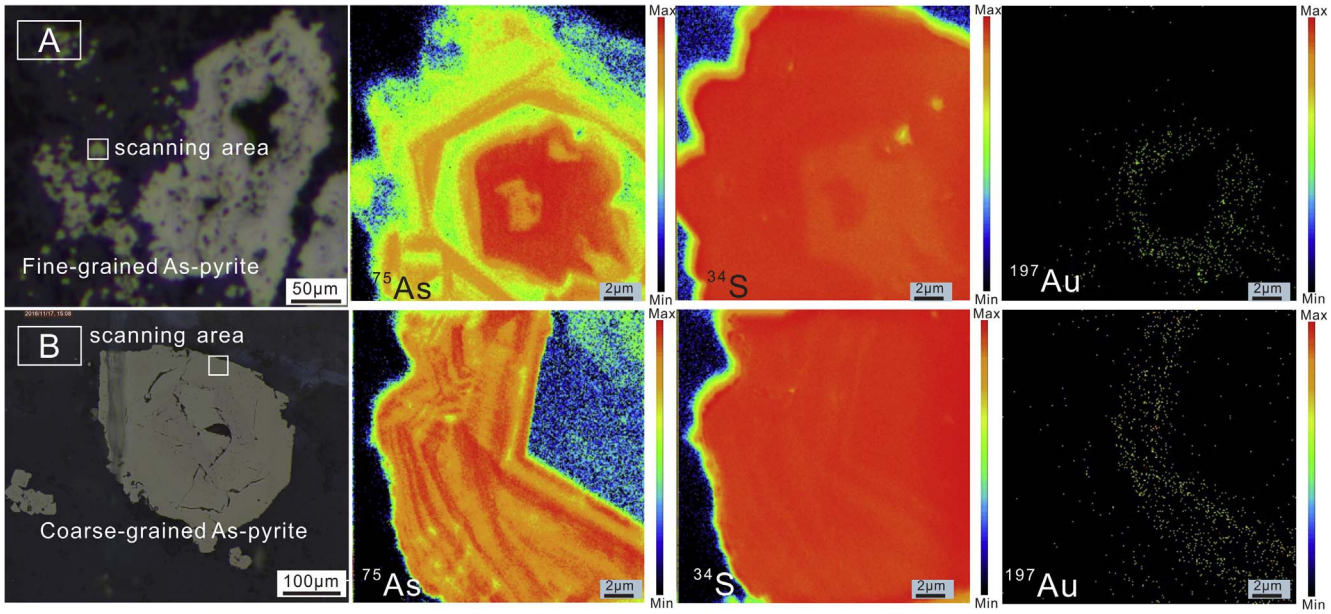

Fig. 11. Geochemical maps of ^{75}As, ^{34}S and ^{197}Au in the Au-bearing pyrite, showing the invisible gold and its relation with the surrounding arsenian pyrite. Note that gold is present in the As-rich section of the zoned pyrite.

206 °C to 325 °C (mean: 262 °C, n = 10). They have $T_{m\text{-}ice}$ ranging from −0.8 to −0.2 °C (mean: 0.6 °C, n = 3), and corresponding salinities of 0.35–1.40 wt% NaCl equiv. (average: 1.06 wt% NaCl equiv). The $T_{m\text{-}ice}$ and T_h of Type-III inclusions are similar to those of Type-Ib inclusions in Fl-IIa (Fig. 13B).

4.3.1.2. Stibnite (Stb-IIa). The Stb-IIa mainly hosts Type-Ia inclusions which have $T_{m\text{-}ice}$ of −9.3 to −0.2 °C (mean: −3.7 °C, n = 35), with corresponding salinities of 0.35 to 13.18 wt% NaCl equiv. (mean: 5.15 wt% NaCl equiv.), mostly 3–5 wt% NaCl equiv. They have homogenization temperatures of 161 °C to 294 °C, mostly 170–250 °C (mean: 220 °C, n = 40) (Fig. 13A). The densities are between 0.824 and 0.946 g/cm^3 (mean: 0.887 g/cm^3, n = 31) (Table 2).

4.3.1.3. Quartz (Qtz-IIa). Type-Ib inclusions commonly occur in Qtz-IIa, but they have not been reported in previous studies. Their $T_{m\text{-}ice}$ vary from of −1.7 to −0.6 °C (mean: −1.3 °C, n = 9), corresponding salinities of 1.06–2.90 wt% NaCl equiv. (mean: 2.16 wt% NaCl equiv.), mostly 2–3 wt% NaCl equiv (Fig. 13B). They homogenized at 174–309 °C (mean: 208 °C, n = 9). The densities range from 0.729 to 0.914 g/cm^3 (average: 0.862 g/cm^3, n = 9).

4.3.2. Late-ore stage (Stage IIb)

Although inclusions are widespread in quartz at this stage (Qtz-IIb), their small sizes make it difficult to measure the ice-melting or homogenization temperatures. Therefore, only the microthermometric data of FIs in Stb-IIb are reported here. Type-Ia inclusions in Stb-IIb have $T_{m\text{-}ice}$ of −3.9 to −0.1 °C (mean: −1.6 °C, n = 48), with corresponding salinities of 0.18–6.30 wt% NaCl equiv. (mean: 2.64 wt% NaCl equiv.), mostly 2.00–5.00 wt% NaCl equiv (Fig. 13D). The homogenization temperatures vary from 113 to 255 °C, mostly 130–200 °C (mean: 175 °C, n = 54) (Fig. 13C). $T_{m\text{-}ice}$ of Type-III inclusions in Stb-IIb range from −2.5 to −1.1 °C (mean: −1.8 °C, n = 5), with corresponding salinities of 1.91 to 4.18 wt% NaCl equiv. (mean: 3.12 wt% NaCl equiv.) (Fig. 13D). They homogenized at 154–183 °C (mean: 169 °C, n = 5). Comparing with the Stb-IIa, the homogenization temperatures of Stb-IIb are lower but have a wider range. The densities range from 0.832 to 0.954 g/cm^3 (mean: 0.916 g/cm^3, n = 53).

4.4. Laser Raman spectroscopy analysis

Representative inclusions were measured using Laser Raman microspectroscopy to constrain their gas compositions. The results show that the vapor phases of FIs in Qtz-IIa are dominated by H_2O (Fig. 14A and B). The vapor phases compositions of Type-Ib in Fl-IIa are primarily H_2O with minor hydrocarbon (1603 cm^{-1}, 2940 cm^{-1} and 3206 cm^{-1}) (Fig. 14C), which is consistent with the results of some previous studies (Ye, 1996; Ye et al., 1997; Xiong et al., 2013; Liu et al., 2016). The vapor phase of Type-III in Fl-IIa consists of mainly H_2O and trace CO_2 (1282 cm^{-1} and 1388 cm^{-1}) (Fig. 14D).

4.5. Sulfur isotopes

The Stb-IIa (from Qtz-Stb ± Fl type ores), Stb-IIb and pyrite (from Qtz-Stb ± Py type ores) were selected for the sulfur isotope study. It is notable that pyrites selected from Qtz-Stb ± Py type ores probably are core-rim pyrite because it is impossible to distinguish the Py-I core and Py-IIb rim during handpicking process. The sulfur isotopic compositions of Qinglong Sb deposit are listed in Table 3 and illustrated in Fig. 15. The $\delta^{34}S_{VCDT}$ values of Stb-IIa (−4.7 to −0.9‰, mean: −3.0 ± 1.3‰, n = 11) and Stb-IIb (−6.6 to −1.5‰, mean: −3.5 ± 1.6‰, n = 12) have an almost uniform range feature, indicating that the sulfur of ore stage from the Qinglong deposit probably derived from a same sources. However, the core-rim pyrites record a wider range of $\delta^{34}S_{VCDT}$ values (−6.0 to 9.7‰, average 1.9 ± 4.4‰; n = 12) (Fig. 15).

5. Discussion

5.1. Sources of sulfur

The ore-stage mineralization at Qinglong is characterized by the presence of stibnite and pyrite but no sulfates, which indicates relatively low fO_2 and H_2S-dominated fluid conditions (Ohmoto, 1972). Previous studies show that temperature has a subtle effect on the H_2S $\delta^{34}S$ values when H_2S is the dominant sulfur species in the ore-forming fluids. Therefore, the $\delta^{34}S$ values of H_2S can represent the $\delta^{34}S$ values of the hydrothermal fluid (Ohmoto and Rye, 1979; Saravanan and Mishra, 2009). In addition, the $\delta^{34}S$ values of pyrite are higher than those of stibnite (Fig. 15). This is consistent with that ^{34}S enrichment follows the

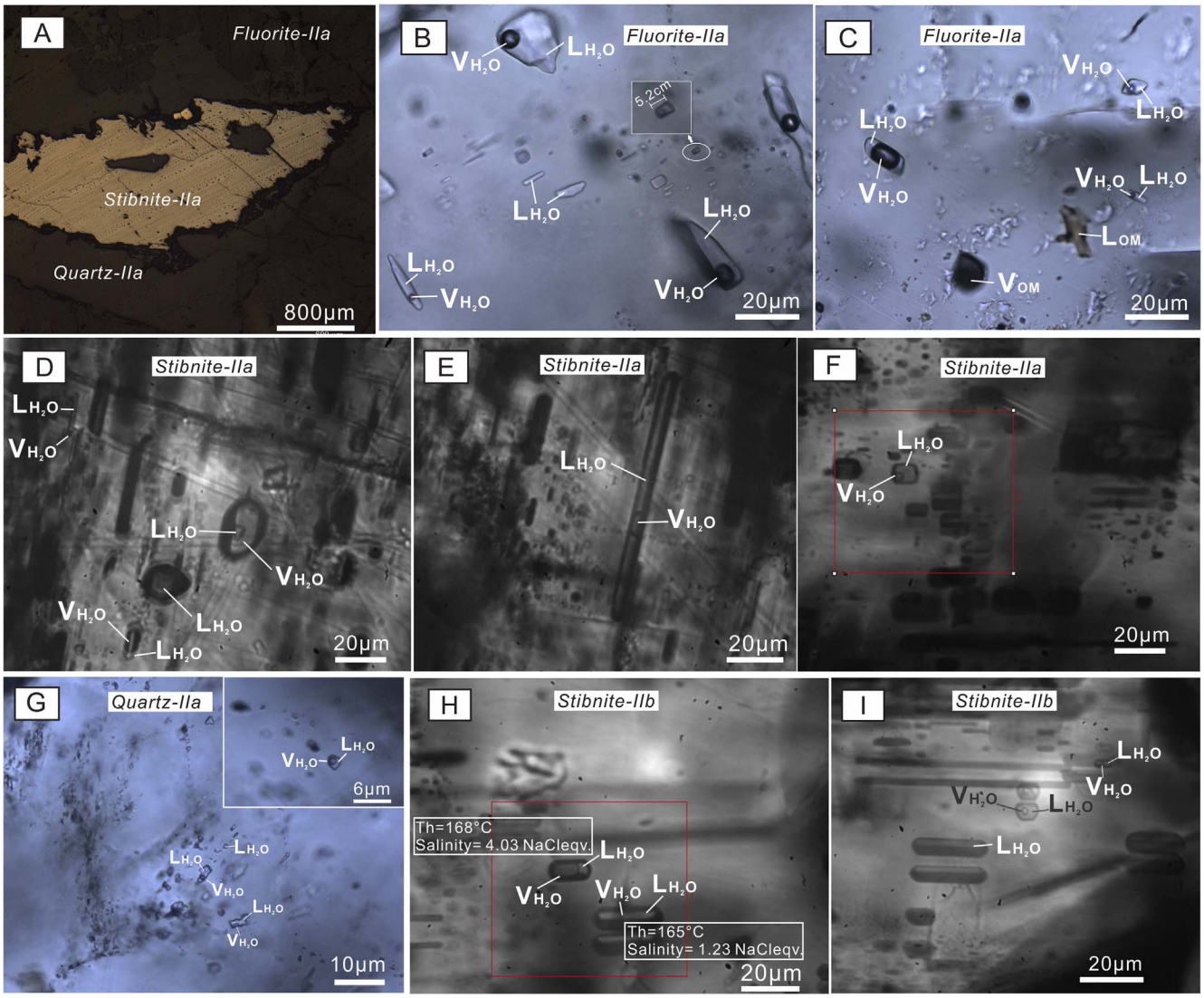

Fig. 12. Photomicrographs of representative FI types at room temperature from the Qinglong deposit. (A) Fluorite (Fl), stibnite (Stb) and quartz (Qtz) in the Qtz-Stb ± Fl type ores. (B) Type-Ib with irregular shape and Type-II inclusions trapped in fluorite-IIa. (C) Type-Ib, -III and -VI inclusions in fluorite-IIa. (D) Type-Ia, -II and -III inclusions in stibnite-IIa. (E, F) Type-Ia inclusions in stibnite-IIa. (G) Type-Ib inclusions in quartz-IIa. (H-I) Type-Ia, -III and/or minor type-II inclusions trapped in stibnite-IIb.

general trend $SO_4^{2-} > SO_3^{-2} > SO_x^o > SO^{2-}$ (Bachinski, 1969; Seal, 2006), and indicates that the isotopic equilibrium between sulfide and H_2S was reached. Using the equilibrium isotopic fractionation factor between stibnite and H_2S ($1000\ln\alpha(Sb_2S_3\text{-}H_2S) = -0.75 \times 10^6/T^2$; Ohmoto and Goldhaber, 1997) and the temperatures of 220 °C and 175 °C (average homogenization temperature of FIs in Stb-IIa and Stb-IIb, respectively), we calculate the $\delta^{34}S_{\Sigma S}$ values of the early-ore stage (−1.6 to 2.2‰, mean: 0.1 ± 1.3‰) and late-ore stage (−2.8 to 2.3, mean: 0.2 ± 1.6‰) ore-forming fluids. The ore-stage stibnite (Stb-IIa and Stb-IIb) has a narrow $\delta^{34}S_{\Sigma S}$ range, indicating that the sulfur in the Qinglong ore-forming fluids may have been dominantly magmatic-derived (−3 to 1‰; Hoefs, 2009).

Table 2
Microthermometric data of the ore-stage fluid inclusions from the Qinglong deposit.

Mineral	Type	Tm-ice (°C)		Salinity (wt% NaCl eqv.)		Th (°C)		D(g/cm3)	
		Range (n)	Ave	Range (n)	Ave	Range (n)	Ave	Range (n)	Ave
The early-ore stage									
Fl-IIa	Ib	−1.8 to −0.6 (16)	−0.8	1.06 to 3.06 (16)	1.48	172 to 344 (26) →L	262	0.715 to 0.911 (19)	0.814
	III	−0.8 to −0.2 (3)	−0.6	0.35 to 1.40 (3)	1.06	206 to 325 (11) →V	262	0.828 to 0.881 (3)	0.885
Stb-IIa	Ia	−9.3 to −0.2 (35)	−3.7	0.35 to 13.18 (35)	5.18	161 to 294 (40) →L	220	0.824 to 0.946 (31)	0.887
Qtz-IIa	Ib	−1.7 to −0.6 (9)	−1.3	1.06 to 2.90 (9)	2.16	174 to 309 (9) →L	208	0.729 to 0.914 (9)	0.862
The late-ore stage									
Stb-IIb	Ia	−3.9 to −0.1 (48)	−1.6	0.18 to 6.30 (48)	2.64	113 to 255 (54) →L	175	0.832 to 0.954 (48)	0.909
	III	−2.5 to −1.1 (5)	−1.8	1.91 to 4.18 (5)	3.12	154 to 183 (5) →V	169	0.898 to 0.941 (5)	0.922

Abbreviations: Tm-ice = final ice-melting temperature; Th = the homogenization temperature; D = density; Fl = fluorite; Qtz = quartz; Stb = stibnite; Ave = average; →L = homogenized to the aqueous phase; →V = homogenized to the vapor phase.

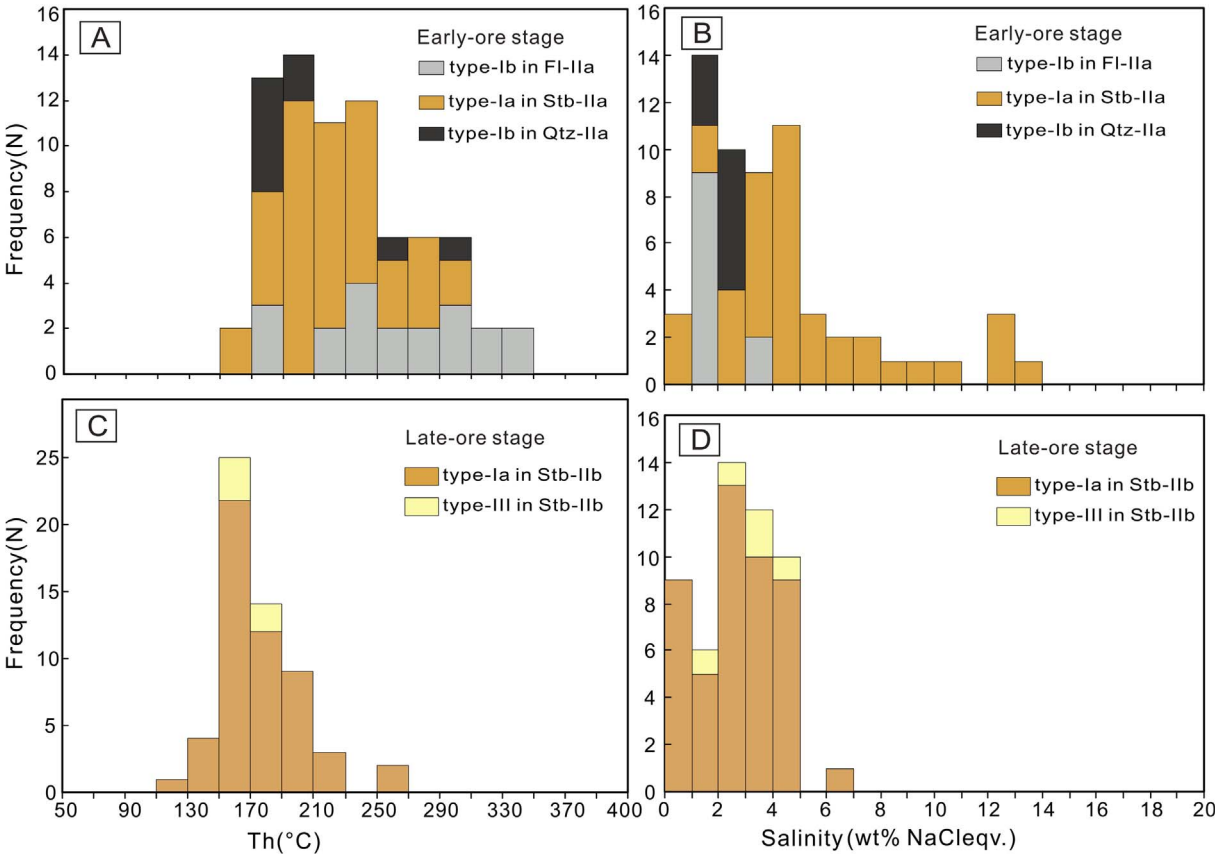

Fig. 13. Histograms of salinities and homogenization temperatures of FIs from Qinglong. Abbreviations: Qtz = quartz; Stb = stibnite; Fl = fluorite.

At Qinglong, the $\delta^{34}S$ values of the zoned pyrite (−6.0 to 6.7‰, mean: 1.9 ± 4.4‰) show a wider range than those of stibnite (−6.6 to −0.9‰). As mentioned above, the zoned pyrite grains generally comprise a Py-I core and a Py-IIb rim (Fig. 10A–C), which suggests that *in-situ* (rather than bulk) sulfur isotope analyses are more effective to constrain the sulfur source of these zoned pyrite. Besides, organic matter was found in both the Qtz-Stb ± Py-type ores and the wall rocks, suggesting that the incorporation of organic sulfur compounds may explain the relatively wide $\delta^{34}S$ range of the zoned pyrite. Although the Carlin-style deposits in the Youjiang basin are widely believed to be magmatic-unrelated, Hou et al. (2016) obtained SHRIMP sulfur isotope compositions of the ore-stage pyrite ($\delta^{34}S$ = −2.6 to 1.5‰) that may reflect a magmatic affinity. The results are similar to our newly-obtained $\delta^{34}S_{\Sigma S}$ values (−2.8 to 2.3‰) of the ore-stage stibnite, which suggests probable magmatic-derived sulfur in the Sb-Au ore-forming fluids at Qinglong.

As mentioned above, no magmatic rocks are documented in the Qinglong Sb mining district. However, felsic dykes are present in some

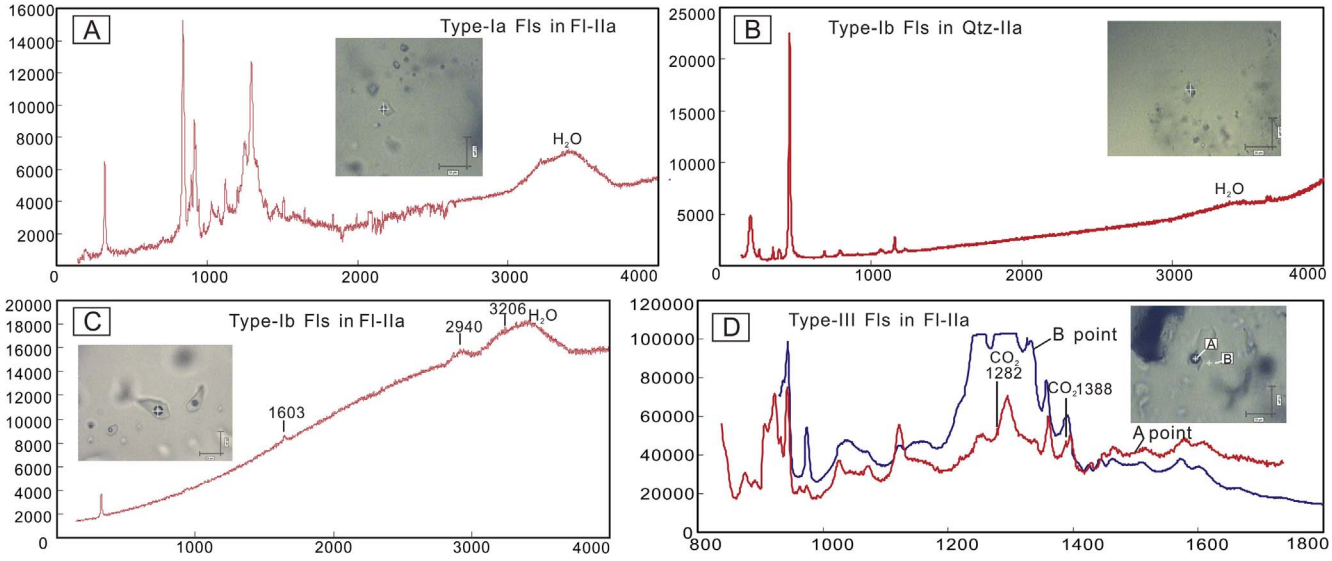

Fig. 14. Representative Raman spectra of FIs in fluorite (A, B, D) and quartz (C) from Qinglong. (A and B) Vapor bubbles are mostly H_2O of Type-Ia FIs in fluorite (Fl) and Type-Ib FIs in quartz (Qtz). (C) Vapor bubbles are mainly consisted of hydrocarbon and H_2O in Type-Ib FIs. (D) Vapor bubbles contain trace CO_2. Abbreviations: Qtz = quartz; Fl = fluorite.

Table 3
Sample data and $\delta^{34}S_{VCDT}$ values of the sulfides from the Qinglong deposit.

Sample No.	Sample types	Location	Minerals	$\delta^{34}S_{VCDT}$ (‰)
Early-ore stage				
DCJ1-3	Coarse-grained	Dachang	Stibnite-IIa	−3.9
DCJ1-8	Drusy crystal	Dachang	Stibnite-IIa	−2.7
DCJ1-8-1	Drusy crystal	Dachang	Stibnite-IIa	−4.1
DCJ1-10	Drusy crystal	Dachang	Stibnite-IIa	−2.2
DCJ1-23	Drusy crystal	Dachang	Stibnite-IIa	−2.8
LBD-13	Drusy crystal	Leibodong	Stibnite-IIa	−1.4
LBC-14	Drusy crystal	Leibodong	Stibnite-IIa	−4.3
LBC-16	Drusy crystal	Leibodong	Stibnite-IIa	−1.7
LBC-18	Drusy crystal	Leibodong	Stibnite-IIa	−4.5
LBC-1	Drusy crystal	Leibodong	Stibnite-IIa	−4.7
GL-1	Disseminated	Gulu	Stibnite-IIa	−0.9
Late-ore stage				
LBC-3	Euhedral-subhedral	Leibodong	Stibnite-IIb	−6.2
LBC-4	Euhedral-subhedral	Leibodong	Stibnite-IIb	−1.5
LBC-5	Euhedral-subhedral	Leibodong	Stibnite-IIb	−6.6
DSC-8	Drusy crystal	Dishuiyan	Stibnite-IIb	−4.4
DSC-1	Fine-grained	Dishuiyan	Stibnite-IIb	−2.4
DSC-2	Fine-grained	Dishuiyan	Stibnite-IIb	−3.6
GL-11	Fine-grained	Gulu	Stibnite-IIb	−2.5
GL-12	Disseminated	Gulu	Stibnite-IIb	−1.5
DC-TK-2	Drusy crystal	Dachang	Stibnite-IIb	−3.8
DC-TK-6	Drusy crystal	Dachang	Stibnite-IIb	−3.1
DC-DJ-1	Fine-grained	Dachang	Stibnite-IIb	−4.3
DC-J1-15	Euhedral-subhedral	Dachang	Stibnite-IIb	−2.5
DC-JS-4	Black, euhedral-subhedral	Dachang	Au-bearing pyrite	1.9
DC-LS-1	Black, subhedral	Dachang	Au-bearing pyrite	0.1
DC-JP-3	Disseminated	Dachang	Au-bearing pyrite	7.8
DC-JP-4	Disseminated	Dachang	Au-bearing pyrite	1.0
DC-J1-1	Black, disseminated	Dachang	Au-bearing pyrite	1.4
DSC-6	Fine-grained	Dishuiyan	Au-bearing pyrite	4.8
GL-5	Coarse-grained	Gulu	Au-bearing pyrite	2.3
GL-2	Coarse-grained	Gulu	Au-bearing pyrite	9.7
GL-3	Coarse-grained	Gulu	Au-bearing pyrite	−3.5
Swp-2	Anhedral	Sanwangpin	Au-bearing pyrite	6.0
LBC-15	Fine-grained	Leibodong	Au-bearing pyrite	−6.0
XS-7	Fine-grained	Xishe	Au-bearing pyrite	−2.4

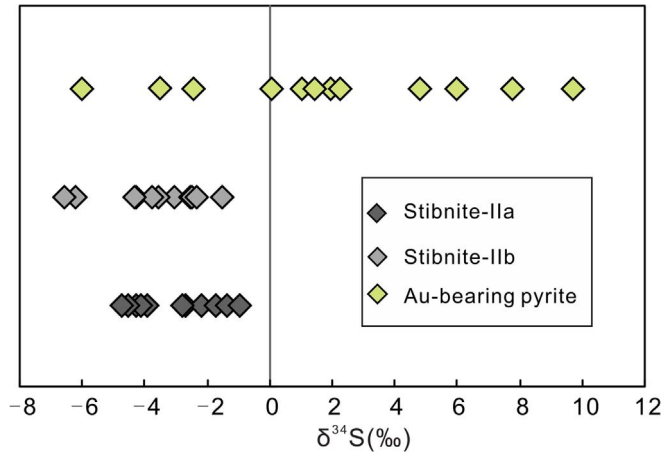

Fig. 15. The $\delta^{34}S_{VCDT}$ values for pre-ore pyrite, early-ore stage stibnite, and late-ore stage stibnite and Au-bearing pyrite from Qinglong.

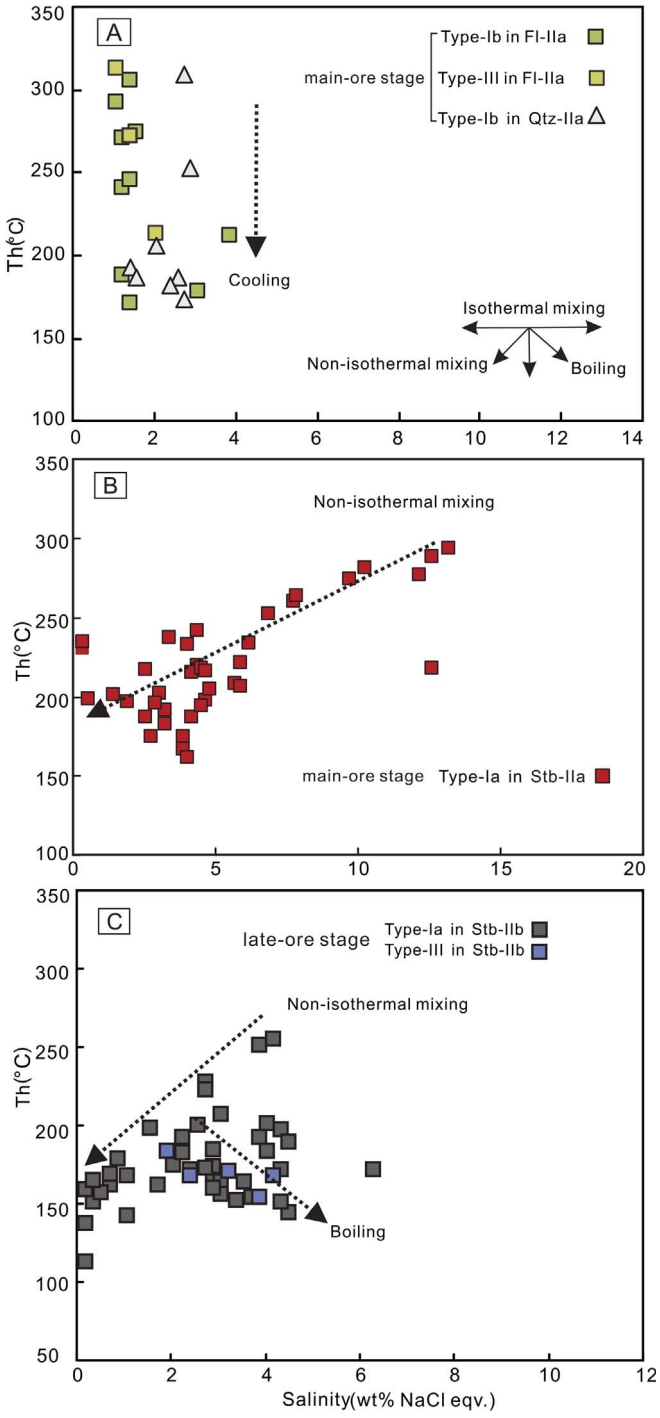

Fig. 16. Homogenization temperature vs. salinity diagram for the FIs in fluorite, quartz and stibnite at the different Qinglong mineralization stages. Abbreviations: Qtz = quartz; Stb = stibnite; Fl = fluorite.

of the Carlin-style Au ore fields nearby Qinglong. These felsic dykes (zircon U-Pb age: 140–130 Ma; Zhu et al., 2016) are broadly syn-mineralized with the Carlin-style Au mineralization (age peak: 148–134 Ma; Li et al., 1995; Liu et al., 2006; Su et al., 2009b) and Qinglong Sb-Au mineralization (fluorite Sm-Nd isochron age: 148–142 Ma; Peng et al., 2003), which suggests a possible metallogenic role of these felsic dykes (e.g., providing the heat to drive the hydrothermal system). Besides, integrated regional gravity and magnetic surveys have delineated 12 possible shallow buried plutons and four large ones in the region (Wang et al., 2009, 2015), suggesting that magmatic contribution to the regional Au-Sb mineralization cannot be

completely precluded (Su et al., 2017).

5.2. Nature of ore-forming fluids

As demonstrated above, Fl-IIa and Qtz-IIa were formed slightly earlier than Stb-IIa (Fig. 7A, C and D). Fluid inclusions from Fl-IIa and Qtz-IIb homogenized at 172–344 °C and 174–309 °C, respectively, whilst their FI salinities are of 0.35–3.06 wt% NaCl equiv. and 1.06–2.90 wt% NaCl equiv. Laser Raman spectrometry identified hydrocarbon in the FIs, indicating the presence of organic matter in the ore-forming fluids. These data indicate that the early-ore stage fluids are characterized by medium to low temperature and low salinities, with the components being H_2O, hydrocarbons and minor CO_2. These features mimic those of the basinal carbonic fluids in the Youjiang basin (Wang et al., 2003; Gu et al., 2007, 2010, 2012). In the salinity vs. Th diagram, the FI salinities of Fl-IIa and Qtz-IIa fall within a narrow range with the homogenization temperature drop, suggesting that fluid cooling was likely responsible for the Fl-IIa and Qtz-IIa precipitation (Fig. 16A).

The Stb-IIa FIs have homogenization temperature and salinities of 161–294 °C and 0.35–13.18 wt% NaCl equiv., respectively (Table 2). In the Th vs. salinity diagram (Fig. 16B), there is a positive homogenization temperature vs. salinity correlation for most of the Stb-IIa Fls, which reveals that a hotter, more saline fluid may have mixed with a cooler, less saline fluid (Wilkinson, 2001; Lu et al., 2004). This is well consistent with the conclusion that fluid mixing may have caused the stibnite precipitation at Qinglong (Su et al., 2015). As supported by the sulfur (this study) and He-Ar isotope (Chen et al., 2016) evidence, the high temperature and salinity fluid may have been magmatic fluids, whereas the low temperature and salinity fluid was likely basinal carbonic fluids.

In the late-ore stage, the Stb-IIb FIs are dominated by Type-Ia. These Fls, and thus the ore-forming fluids they represent, were characterized by low temperatures (113–255 °C, mainly 130–200 °C), low salinities (0.18–6.30 (mainly 2.00–5.00)wt% NaCl equiv.) (Table 2; Fig. 13C and D). In the Th vs. salinity diagram (Fig. 16C), the FI salinities largely decrease with decreasing homogenization temperatures, suggesting that the fluid mixing may have occurred in the late-ore stage. Furthermore, the hydrogen and oxygen isotopic compositions of the Stage IIb veined quartz also suggest meteoric water incursion into the hydrothermal system (Chen, 1992; Ye, 1996). On the other hand, the homogenization temperatures of Type-Ia (163–166 °C) and the coexisting Type-III FIs (161–170 °C) in Stb-IIb are similar, yet their salinities (1.06–1.57 wt% NaCl equiv. and 3.87–4.03 wt% NaCl equiv., respectively) are different. During the heating runs, Type-Ia FIs homogenized by the disappearance of the vapor bubble, but Type-III FIs homogenized by vanishing the liquid phase. These features suggest that fluid boiling may have locally contributed to the Stb-IIb precipitation, although it was unlikely to be the key trigger because these two FI types are scarce compared to the other FI types.

5.3. Metal transport and deposition mechanism

The solubility of Sb in hydrothermal systems is mainly controlled by temperature, pH, $fO_{2(g)}$ and $fS_{2(g)}$ (Williams-Jones and Norman, 1997). Stibnite is the dominant ore mineral in most primary Sb deposits (Williams-Jones and Norman, 1997). At Qinglong, the fS_2 and fO_2 values are estimated using the fS_2-fO_2-temperature phase diagram (Simon et al., 1999; Xie et al., 2017). Log $fS_{2(g)}$ is inferred to be ca. −14 to −17 by using the ore mineral assemblage (i.e., stibnite) and the early-ore stage mineralization temperatures (FI homogenization temperatures of Stb-IIa: 170–250 °C) (Fig. 17; Table 4). Similarly, by using the late-ore stage mineral assemblage (stibnite + arsenian pyrite) and mineralization temperatures (FI homogenization temperatures of Stb-IIb: 130–200 °C), the log $fS_{2(g)}$ values are estimated to be ca. −14 to −20 (Fig. 17). Based on such log $fS_{2(g)}$ values and the stable mineral assemblages, log $fO_{2(g)}$ of the early-ore and late-ore stages are estimated to be ca. −37 to −45 (Fig. 18A) and −46 to −55 (Fig. 18B), respectively.

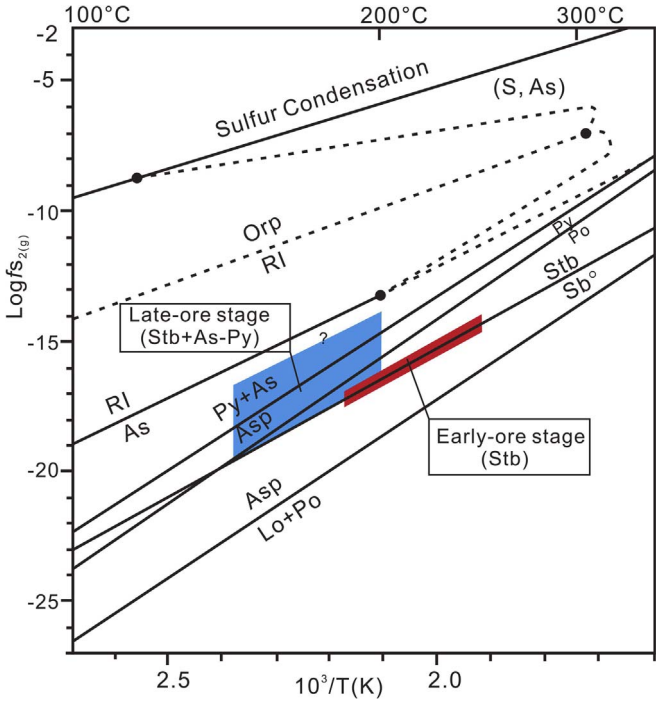

Fig. 17. Temperature vs. log$fS_{2(g)}$ diagram showing stability fields of minerals assemblages from early-ore and late-ore stage at Qinglong (modified from Simon et al., 1999). Red shade represents the stability field of the early-ore stage stibnite, and blue shade represents the stability field of the late-ore stage stibnite + arsenian pyrite assemblage. Boundary with question mark denotes the uncertainty of the exact sulfur fugacity boundary, which should lie somewhere between the two adjacent boundaries. Abbreviations: As = arsenic, Asp = arsenopyrite, Lo = loellingite, Orp = orpiment, Po = pyrrhotite, Py = pyrite, Rl = realgar, S = sulfur, Sb^0 = native antimony, Stb = stibnite. (For interpretation of the references to colour in this figure legend, the reader is referred to the web version of this article.)

Table 4
Physicochemical parameters of the Qinglong deposit.

Physicochemical parameter	Early-ore stage	Late-ore stage
Mineral assemblages	stibnite	stibnite + arsenian pyrite
Temperature (°C)	161 to 294 (mainly 170 to 250)	113 to 255 (mainly 130 to 200)
Log $fS_{2(g)}$	−14 to −17	−14 to −20
Log $fO_{2(g)}$	−37 to −45	−46 to −55
pH	< 5 (inferred by kaolinite; Reyes, 1991; Hedenquist et al., 1996, 2000)	5~7 (inferred by illite; Reyes, 1991; Hedenquist et al., 1996, 2000)

Understanding of the metal speciation in hydrothermal fluids is necessary to determine the metal solubility (Williams-Jones and Norman, 1997). Antimony is mainly transported as hydroxyl (e.g., Sb (OH)0 3) (Wood et al., 1987; Shikina and Zotov, 1991) and bisulfide (e.g., Sb_2S_2(OH)0 2) complexes under low pH and medium fO_2 (Krupp, 1988; Spycher and Reed, 1989), as hydroxybisulfide (e.g., HSb_2S- 4) complexes under nearly neutral pH (6.0–7.7) and medium fO_2 (Krupp, 1988; Williams-Jones and Norman, 1997), and Sb(OH)- 4 under high pH (> 10) (Williams-Jones and Norman, 1997). Different types of argillic alteration minerals (e.g., kaolinite, dickite and illite) are indicative of the pH and/or redox conditions (Reyes, 1991; Hedenquist et al., 1996, 2000). The presence of kaolinite (a major gangue mineral) and the absence of secondary carbonate minerals in the early-ore stage

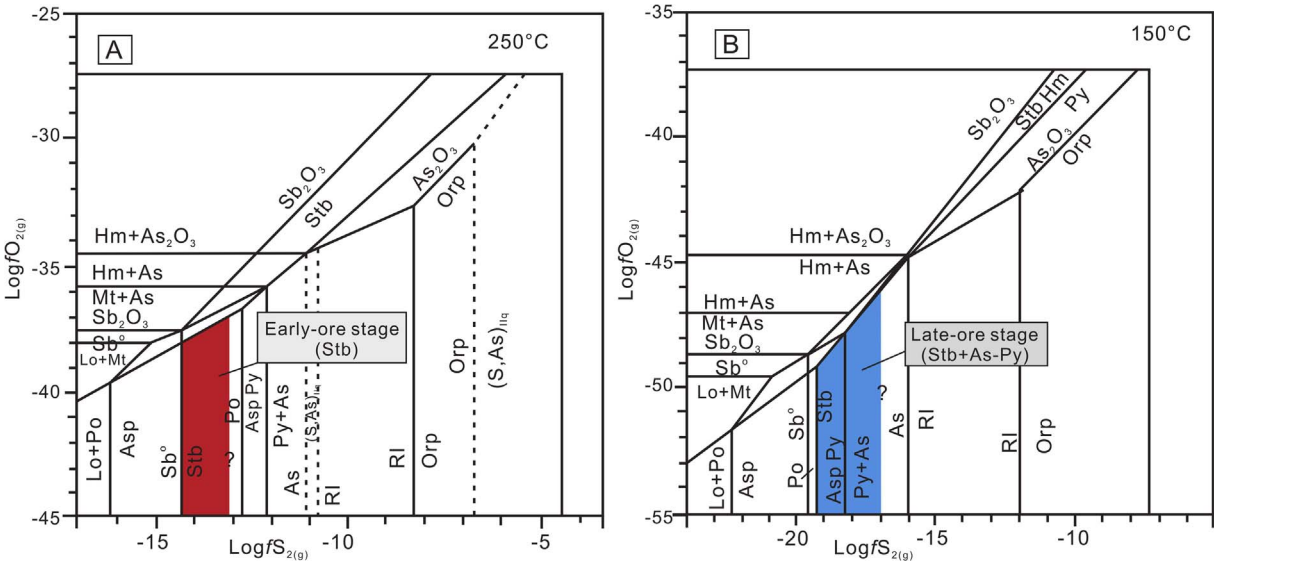

Fig. 18. (A) Log$fS_{2(g)}$ vs. log$fO_{2(g)}$ diagram, showing the stability fields of stibnite (red field) in the early-ore stage at 250 °C for the Qinglong deposit (modified from Simon et al., 1999). The exact location of the sulfur fugacity boundary (with a question mark) is unknown, but it should lie between the two adjacent boundaries. (B) Log$fS_{2(g)}$ vs. log$fO_{2(g)}$ diagram, showing the stability fields of stibnite + arsenian pyrite assemblages (blue field) in the late-ore stage at 150 °C (modified from Simon et al., 1999). Abbreviations as in Fig. 17, and Hm = hematite, Mt = magnetite. (For interpretation of the references to colour in this figure legend, the reader is referred to the web version of this article.)

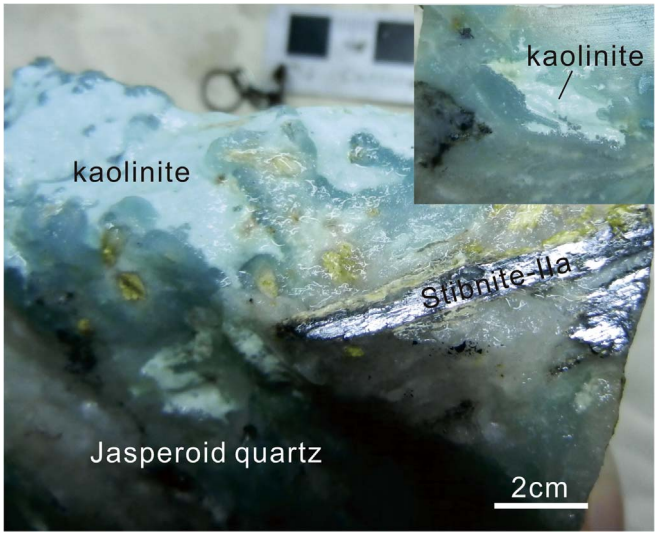

Fig. 19. Hydrothermal kaolinite coexists with jasperoid quartz and stibnite, suggesting that the early-ore stage hydrothermal fluids were likely acidic.

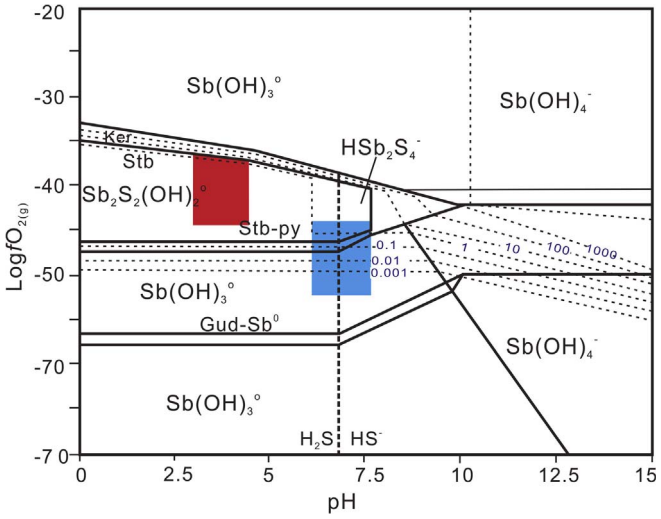

Fig. 20. Log $fO_{2(g)}$ versus pH diagram at 200 °C and Σαs = 0.01, showing contours of Sb solubility in ppm (black dashed lines). Also shown are the distribution of the dominant Sb species (note that the species $HSb_2S_4^-$ is limited to pH conditions between 6.0 and 7.7 and $Sb(OH)_4^-$ to pH > 10) and stability fields of minerals (black solid lines) in the system Fe-Sb-S-O (modified from Williams-Jones and Norman, 1997). The fields of early-ore stage and late-ore stage minerals in the Qinglong deposit are shown. Red represents the stability field of early-ore stage stibnite, and blue represents the stability field of late-ore-stage minerals stibnite and arsenian pyrite. Gud = gudmundite, Ker = kermesite, Py = pyrite, Stb = stibnite, Sb^0 = native antimony. (For interpretation of the references to colour in this figure legend, the reader is referred to the web version of this article.)

at Qinglong (Fig. 19) suggest that the ore-forming fluids were likely acidic and low temperature (170–250 °C). In contrast, abundant illite is present in the late-ore stage (Fig. 10D), indicating that the ore-forming fluids had nearly neutral pH. Therefore, Sb was likely transported as $Sb_2S_2(OH)0$ 2 and HSb_2S- 4 in the early-ore and late-ore stage, respectively (Fig. 20). Gold mineralization in the late-ore stage is similar to the Carlin-style Au deposits in southwestern Guizhou (Su et al., 2008, 2012), e.g., the absence of native gold. This suggests that the Au was likely transported as $AuHS^0$, similar with typical Carlin-style Au deposits (Su et al., 2012; Reich et al., 2013; Deditius et al., 2014).

Hagemann and Lüders (2003) concluded that stibnite is highly soluble in most hydrothermal fluids at about 300 °C, regardless of their pH, fO_2 or fS_2 conditions. Thus, substantial physicochemical changes in the hydrothermal system are required to precipitate the stibnite. For Qinglong, we propose that the fluid-mixing between a high-temperature, high-salinity magmatic fluid and a cooler, low-salinity basinal carbonic fluid in the early-ore stage (Fig. 21) may have led to a significant drop in temperature (from 294 °C to 161 °C) and log fO_2 (from −37 to −45). These changes may have significantly reduced the Sb solubility from 100 s of ppm to 0.1 ppm (Fig. 20), which caused the abundant stibnite precipitation. In the late-ore stage, Sb is likely transported as HSb_2S- 4 and the Sb solubility was around 10 s ppm (Fig. 20). We suggest that when the ore-forming fluids were transported to the organic-rich middle and upper units of the Dachang layer, the log fO_2 and temperature may have further dropped by the interactions with the organic matter and by meteoric water incursion, which led to further (but less important) stibnite precipitation (Fig. 21). The extensive stibnite precipitation may have reduced the H_2S concentration in the ore-forming fluids, thereby destabilizing the $AuHS^0$ complexes in the ore-forming fluids, leading to gold mineralization (Krupp, 1988; Su

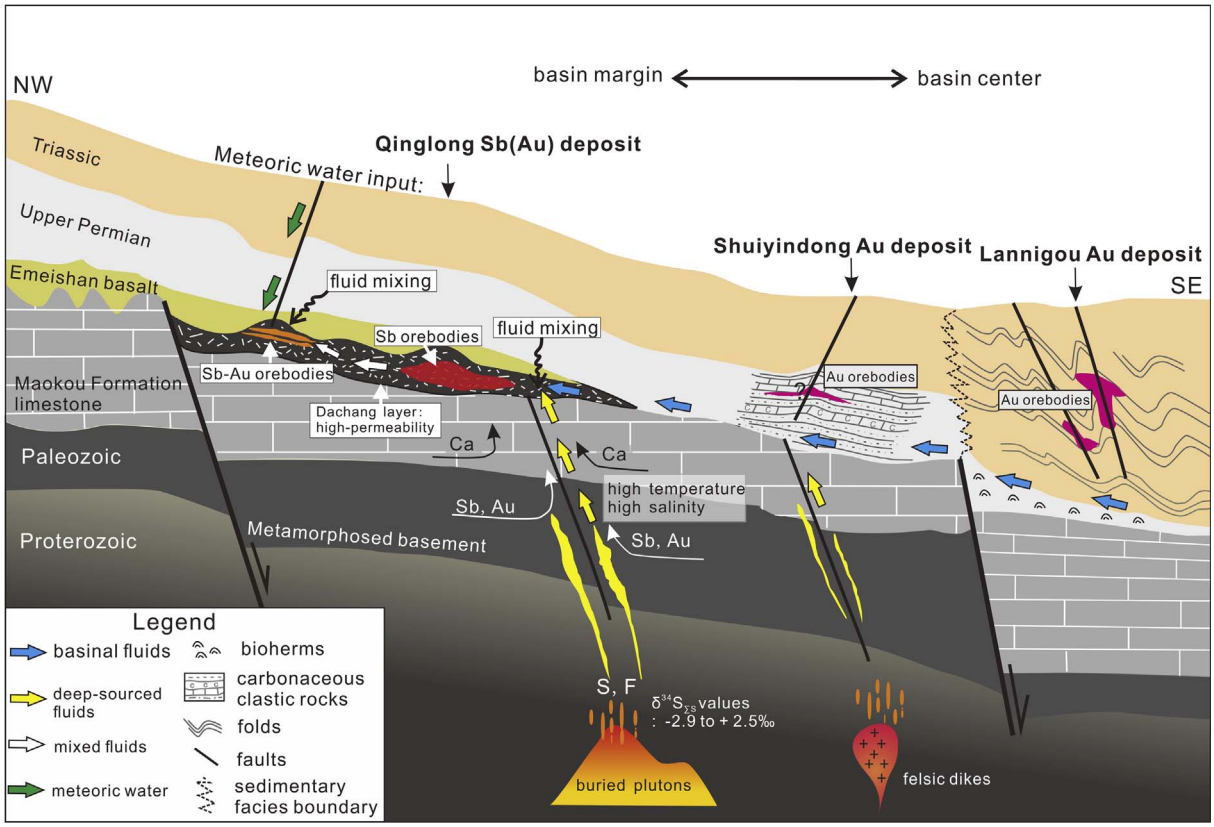

Fig. 21. Schematic metallogenic model for the Qinglong Sb-(Au) deposit and the Carlin-style Au deposits nearby.

et al., 2012).

6. Conclusions

(1) The Qinglong deposit is a Sb-(Au) deposit in the Youjiang basin (SW China), comprising an early Sb (Qtz-Stb ± Fl-type ores) and late Sb-Au (Qtz-Stb ± Py-type ores) mineralization phase.
(2) Fluid inclusion petrographic, infrared microthermometric and laser-Raman analyses reveal that the ore-forming fluids contain mainly H_2O + NaCl + hydrocarbon ± CO_2.
(3) The early-ore stage hydrothermal fluids are medium to low temperatures (161–294 °C), medium to low salinities (0.35–13.18 wt% NaCl equiv.) and acidic, whereas the late-ore stage hydrothermal fluids are low temperatures (113–255 °C), low salinities (0.18–6.30 wt% NaCl equiv.) and have nearly neutral pH.
(4) $\delta^{34}S_{\Sigma S}$ values of the ore-stage stibnite fall inside a narrow range clustering around zero (−2.8 to 2.3‰), indicating a predominantly magmatic sulfur origin.
(5) Fluids mixing may have caused significant temperature and fO_2 drop, which reduced the stibnite solubility and triggered its precipitation. Extensive stibnite deposition had likely depleted the H_2S concentrations in the ore-forming fluids, thereby destabilizing the $AuHS^0$ complexes and caused the Au-bearing arsenian pyrite precipitation.

Acknowledgments

This study was financially supported by the Foundation and Public-Welfare Project of Guizhou (201534), National Natural Science Foundation of China (41503030), Project of Science and Technology Cooperation of Guizhou (20157663, 20152032), and the Project of Young Scientific Talent of Guizhou (2016117). We thank Cai Jia-li and Qin Chao-jian for the fluid inclusion and laser Raman spectroscopy analyses. Special thanks are due to the staffs of the Qinglong mining district for their field support. Pro. Su Wen-Chao and two anonymous reviewers are thanked for their constructive comments and suggestions. Cenozoic Geoscience Editing & Consultancy (Australia) is acknowledged for its scientific and language editing service.

References

Bachinski, D.J., 1969. Bond strength and sulfur isotopic fractionation in coexisting sulfides. Econ. Geol. 64, 56–65.
Brown, P.E., Lamb, W.M., 1989. P-V-T properties of fluids in the system H_2O ± CO_2 ± NaCl: new graphical presentations and implications for fluid inclusion studies. Geochim. Cosmochim. Acta. 53, 1209–1221.
Buchholz, P., Oberthür, T., Lüders, V., Wilkinson, J., 2007. Multistage Au-As-Sb mineralization and crustal-scale fluid evolution in the Kwekwe district, Midlands greenstone belt, Zimbabwe: a combined geochemical, mineralogical, stable isotope, and fluid inclusion study. Econ. Geol. 102, 347–378.
Chen, D.Y., 1992. The low-temperature geochemical characteristics of ore-forming fluid of the Dachang antimony deposit in Qinglong. Bull Mineral. Petrol Geochem. 11 (1), 3–5 (in Chinese).
Chen, J., Yang, R.D., Zheng, L.L., Gao, J.B., Wei, H.R., 2014. A research on the genesis of the conglomerate of dachang layer of middle permian in qinglong, Guizhou. Geol Rev. 60 (6), 1309–1322 (in Chinese with English abstract).
Chen, M.H., Mao, J.W., Li, C., Zhang, Z.Q., Dang, Y., 2015. Re–Os isochron ages for arsenopyrite from Carlin-like gold deposits in the Yunnan–Guizhou–Guangxi "golden triangle", southwestern China. Ore Geol. Rev. 64, 316–327.
Chen, M.H., Huang, Q.W., Hu, Y., Chen, Z.Y., Zhang, W., 2009. Genetic types of phyllosilicate (micas) and its ^{40}Ar-^{39}Ar dating in Lannigou gold deposit, Guizhou province, China. Acta Mineral. Sin. 29, 353–362 (in Chinese with English abstract).
Chen, X., Su, W.C., Huang, Y., 2016. He and Ar isotope geochemistry of ore-forming fluids for the Qinglong Sb deposit in Guizhou Province, China. Acta Petrol Sin. 32 (11), 3312–3320.
Deditius, A.P., Reich, M., Kelser, S.E., Utsunomiya, S., Chryssoulis, S.L., Walshe, J., Ewing, R.C., 2014. The coupled geochemistry of Au and As in pyrite from hydrothermal ore deposits. Geochim. Cosmochim. Acta. 140, 644–670.
Deditius, A.P., Utsunomiya, S., Renock, D., Ewing, R.C., Ramana, C.V., Becker, U., Kesler, S.E., 2008. A proposed new type of arsenian pyrite: composition, nanostructure and geological significance. Geochim. Cosmochim. Acta. 72, 2919–2933.
Ge, X., Su, W.C., Zhu, L.Y., Wu, L.Y., 2011. A study on the influence of infrared light source intensity on salinity of fluid inclusion in opaque mineral by using infrared microthermometry: in the case of stibnite. Acta Mineral. Sin. 31, 366–371 (in Chinese

with English abstract).
Gu, X.X., Zhang, Y.M., Li, B.H., Dong, S.Y., Xue, C.J., Fu, S.H., 2012. Hydrocarbon and ore-bearing basinal fluids: a possible link between gold mineralization and hydrocarbon accumulation in the Youjiang basin, south China. Mineral. Deposita. 47 (6), 663–682.
Gu, X.X., Li, B.H., Xu, S.H., Fu, S.H., Dong, S.Y., 2007. Characteristics of hydrocarbon-bearing ore-forming fluids in the Youjiang Basin, South China: implications for hydrocarbon accumulation and ore mineralization1. Earth Sci. Front. 14 (5), 133–146.
Gu, X.X., Zhang, Y.M., Li, B.H., Xue, C.J., Dong, S.Y., Fu, S.H., Liu, L., Wu, C.Y., 2010. The coupling relationship between metallization and hydrocarbon accumulation in sedimentary basins. Earth Sci. Front. 17, 83–105 (in Chinese with English abstract).
Guizhou BGMR (Bureau of Geology and Mineral Resources), 1987. Regional Geology of Guizhou Province. Geol. Publ. House, Beijing, pp. 1–666 (in Chinese).
Guo, J.H., 2000. Relationship between ultramicro-grained gold mineralization and magmatism in northwest Guangxi Province, China. J. Precious Metallic. Geol. 9, 133–143 (in Chinese with English abstract).
Hagemann, S.G., Lüders, V., 2003. P-T-X conditions of hydrothermal fluids and precipitation mechanism of stibnite-gold mineralization at the Wiluna lode-gold deposits, western Australia: conventional and infrared microthermometric constraints. Mineral. Deposita. 38 (8), 936–952.
Hedenquist, J.W., Arribas, A., Gonzalez-Urien, E., 2000. Exploration for epithermal gold deposits. In: Hagemann, S.G. and Brown, P.E. (Eds): Gold in 2000, Rev. Econ. Geol. 13, pp. 245–277.
Hedenquist, J.W., Izawa, E., Arribas, A., White, N.C., 1996. Epithermal gold deposits: styles, characteristics and exploration. J. Soc. Resour. Geol. Spec. Publ. 1, 1–16.
Hoefs J., 2009. Stable isotope geochemistry. Springer Berlin Heidelberg, 26(12), pp. 573–576.
Hou, L., Peng, H.J., Ding, J., Zhang, J.R., Zhu, S.B., Wu, S.Y., Ouyang, H.G., 2016. Textures and in situ chemical and isotopic analyses of pyrite, Huijiabao trend, Youjiang basin, China: implications for paragenesis and source of sulfur. Econ. Geol. 111 (2), 331–353.
Hu, R., Zhou, M., 2012. Multiple Mesozoic mineralization events in South China—an introduction to the thematic issue. Mineral. Deposita. 47 (6), 579–588.
Hu, R.Z., Peng, J.T., Ma, D.S., Su, W.C., Shi, C.H., Bi, X.W., Tu, G.Z., 2007. Epoch of large-scale low-temperature mineralization in southwestern Yangtze massif. Miner. Deposits. 26 (6), 583–596 (in Chinese with English abstract).
Hu, R.Z., Su, W.C., Bi, X.W., Tu, G.Z., Hofstra, A.H., 2002. Geology and geochemistry of Carlin-type gold deposits in China. Mineral. Deposita. 37 (37), 378–392.
Hu, R.Z., Su, W.C., Bi, X.W., Li, Z.Q., 1995. A possible evolution way of ore-forming hydrothermal fluid for the Carlin-type gold deposits in the Yunnan–Guizhou–Guangxi triangle area. Acta Mineral. Sin. 15, 144–149 (in Chinese with English abstract).
Huang, Y.Q., Cui, Y.Q., 2001. The relationship between magmatic rocks and gold mineralization of Mingshan Gold deposit of Lingyun. Guangxi. Guangxi Geol. 4, 22–28 (in Chinese with English abstract).
Huang, Z., Hu, R., Su, W., Wen, H., Liu, S., Fu, Y., 2011. A study on the Large-scale low-temperature metallogenic domain in southwestern China-Significance, history and new progress. Acta Mineral. Sin. 31 (3), 309–314 (in Chinese with English abstract).
Krupp, R.E., 1988. Solubility of stibnite in hydrogen sulfide solutions speciation and equilibrium constants from 25 to 350°C. Geochim. Cosmochim. Acta. 52, 3005–3015.
Li, S., Wang, D., Liang, T., Qu, W., Ying, L., 2008. Metallogenic epochs of the Damingshan tungsten deposit in Guangxi and its prospecting potential. Acta Geol. Sinica 82, 873–879 (in Chinese with English abstract).
Li, Y.Q., Pang, B.C., Yang, F., Zhang, D.W., Zeng, Q.F., Liu, X., 2014. Geochemical characteristics and metallogenic significance of quartz porphyry in Liaotun gold deposit, Bama County, Guangxi. Geoscience 6, 1138–1150 (in Chinese with English abstract).
Li, Z.P., Peters, S.G., 1998. Comparative geology and geochemistry of sedimentary-rock hosted (Carlin-type) gold deposits in the People's Republic of China and in Nevada, USA. U.S. Department of the Interior, U.S. Geol. Survey. Open-File Report 98–466, 1–91.
Li, Z.Q., Chen, S.D., Wang, J.Z., Li, F.C., Wang, G.T., 1995. Isotope geochemistry of Jinya disseminated gold deposit in western Guangxi. J. Miner. Petrol. 15, 66–72 (in Chinese with English abstract).
Liao, B.L., 2013. Study of petrology and geochemistry of the Permian alkaline basalt in Guizhou Province. Ph.D. Dissertation. China Univ. Geosci. Beijing, pp. 1–76 (in Chinese with English abstract).
Liu, L., Hu, Y.Z., Zhang, G.Q., 2016. Raman spectral characteristics of Qinglong antimony ore field paleo-oil reservoir bitumen and hydrocarbon inclusions. Geol Rev. 62 (4), 1011–1020 (in Chinese with English abstract).
Liu, P., Li, P.G., Ma, R., Han, Z.H., Yang, G.L., Ye, D.S., 2006. A gold deposit associated with pyroclastic rock and hydrothermal exhalation: Nibao gold deposit in Guizhou province, China. Miner. Deposits 1, 101–110 (in Chinese with English abstract).
Liu, S., Su, W., Hu, R., Feng, C., Gao, S., Coulson, I.M., Wang, T., Feng, G., Tao, Y., Xia, Y., 2010. Geochronological and geochemical constraints on the petrogenesis of alkaline ultramafic dikes from southwest Guizhou Province, SW China. Lithos 114, 253–264.
Lu, H.Z., Fan, H.R., Ni, P., Ou, G.X., Shen, K., Zhang, W.H., 2004. Fluid Inclusions. In: Science Press, Beijing, pp. 1–274 (in Chinese).
Ma, J., Pang, B., Li, P., Yang, B., Zhao, J., 2013. Geochemical characteristics of the quartz porphyry and its geological implications, northwest Guangxi, China. Acta Mineral. Sin. 33 (S2), 165 (in Chinese).
Mao, J.W., Cheng, Y.B., Chen, M.H., Pirajno, F., 2013. Major types and time–space distribution of Mesozoic ore deposits in South China and their geodynamic settings. Miner. Deposita 48, 267–294.
Ni, P., Wang, X.D., Wang, G.G., Huang, J.B., Pan, J.Y., Wang, T.G., 2015. An infrared microthermometric study of fluid inclusions in coexisting quartz and wolframite from Late Mesozoic tungsten deposits in the Gannan metallogenic belt, South China. Ore Geol. Rev. 65, 1062–1077.
Ohmoto, H., 1972. Systematics of sulfur and carbon isotopes in hydrothermal ore deposits. Econ. Geol. 67 (5), 551–578.
Ohmoto, H., Goldhaber, M.B., 1997. Sulfur and Carbon Isotopes. In: Barnes, H.L. (Ed.), Geochemistry of Hydrothermal Ore Deposits, third ed. John Wiley, New York, pp. 517–611.
Ohmoto, H., Rye, R.O., 1979. Isotopes of sulfur and carbon. In: Barnes, H.L. (Ed.), Geochemistry of Hydrothermal Ore Deposits, Second ed. Wiley, New York, pp. 509–567.
Peng, J.T., Hu, R.Z., Jiang, G.H., 2003. Samarium-Neodymium isotope system of fluorites from the Qinglong antimony deposit, Guizhou Province: constraints on the mineralizing age ore-forming materials' sources. Acta Petrol Sin. 19 (4), 785–791 (in Chinese with English abstract).
Peters, S.G., Huang, J.Z., Li, Z.P., Jing, C.G., 2007. Sedimentary rock-hosted Au deposits of the Dian–Qian–Gui area, Guizhou, and Yunnan Provinces, and Guangxi District, China. Ore Geol. Rev. 31, 170–204.
Pi, Q.H., Hu, R.Z., Xiong, B., Li, Q., Zhong, R.C., 2017. In situ SIMS U-Pb dating of hydrothermal rutile: reliable age for the Zhesang Carlin-type gold deposit in the golden triangle region, SW China. Miner. Deposita. 1–12.
Reich, M., Deditius, A., Chryssoulis, S., Li, J.W., Ma, C.Q., Parada, M.A., Barra, F., Mittermayr, F., 2013. Pyrite as a record of hydrothermal fluid evolution in a porphyry copper system: a SIMS/EMPA trace element study. Geochim. Cosmochim. Acta. 104, 42–62.
Reich, M., Kesler, S.E., Utsunomiya, S., Palenik, C.S., Chryssoulis, S.L., Ewing, R.C., 2005. Solubility of gold in arsenian pyrite. Geochim. Cosmochim. Acta. 69, 2781–2796.
Reyes, A.G., 1991. Mineralogy, distribution and origin of acid alteration in Philippine geothermal systems. Geological Survey of Japan, Special Report: Chishitsu Chosasho Tokubetsu Hokoku 277, 59–66.
Roedder, E., 1984. Fluid inclusions. Miner. Soc. Am. Rev. Miner. 12, 1–644.
Saravanan, C.S., Mishra, B., 2009. Uniformity in sulfur isotope composition in the orogenic gold deposits from the Dharwar Craton, southern India. Miner. Deposita. 44 (5), 597–605.
Seal, R.R., 2006. Sulfur isotope geochemistry of sulfide minerals. Rev. Min. Geochem. 61 (1), 633–677.
Shikina, N.D., Zotov, A.V., 1991. Thermodynamic parameters of Sb(OH)0 3 (sol) up to 723.15K and 1000 bar. Geochem Int. 28, 97–103.
Simon, G., Kesler, S.E., Chryssoulis, S., 1999. Geochemistry and textures of gold-bearing arsenian pyrite, Twin Creeks, Nevada: implications for deposition of gold in Carlin-type deposits. Econ. Geol. 94, 405–422.
Spycher, N.F., Reed, M.H., 1989. As (III) and Sb (III) sulfide complexes: an evaluation of stoichiometry and stability from existing experimental data. Geochim. Cosmochim. Acta. 53, 2185–2194.
Su, W.C., Xia, B., Zhang, H.T., Zhang, X.C., Hu, R.Z., 2008. Visible gold in arsenian pyrite at the Shuiyindong Carlin-type gold deposit, Guizhou, China: implications for the environment and processes of ore formation. Ore Geol. Rev. 33 (3–4), 667–679.
Su, W.C., Heinrich, C.A., Pettke, T., Zhang, X.C., Hu, R.Z., Xia, B., 2009a. Sediment-hosted gold deposits in Guizhou, China: products of wall-rock sulfidation by deep crustal fluids. Econ. Geol. 104 (1), 73–93.
Su, W.C., Hu, R.Z., Xia, B., Xia, Y., Liu, Y.P., 2009b. Calcite Sm-Nd isochron age of the Shuiyindong Carlin-type gold deposit, Guizhou, China. Chem. Geol. 258 (3–4), 269–274.
Su, W.C., Zhang, H.T., Hu, R.Z., Ge, X., Xia, B., Chen, Y.Y., Zhu, C., 2012. Mineralogy and geochemistry of gold-bearing arsenian pyrite from the Shuiyindong Carlin-type gold deposit, Guizhou, China: implications for gold depositional processes. Mineral. Deposita. 47 (6), 653–662.
Su, W.C., Zhu, L.Y., Ge, X., Shen, N.P., Zhang, X.C., Hu, R.Z., 2015. Infrared microthermometry of fluid inclusions in stibnite from the Dachang antimony deposit, Guizhou. Acta Petrol Sin. 31 (4), 918–924 (in Chinese with English abstract).
Su, W.C., Dong, W.D., Zhang, X.C., Shen, N.P., Hu, R.Z., Hofstra, A.H., Cheng, L.Z., Xia, Y., Yang, K.Y., 2017. Carlin-style gold deposits in the Dian-Qian-Gui "Golden Triangle" of Southwest China. Rev. Econ. Geol in press.
Sun, X.M., Mo, R.W., Zhai, W., Wei, H.X., Liang, Y.H., Zhang, X.G., Yi, J.Z., 2014. Infrared fluid inclusion microthemometry on stibnite from Shalagang antimony ore in southern Tibet, China. Acta Petrol Sin. 30 (1), 189–198 (in Chinese with English abstract).
Tan, Q.P., Xia, Y., Xie, Z.J., Yan, J., 2015. Migration paths and precipitation mechanisms of ore-forming fluids at the Shuiyindong Carlin-type gold deposit, Guizhou, China. Ore Geol. Rev. 69, 140–156.
Wang, D.H., Chen, Y.C., Chen, W., Sang, H.Q., Li, H.Q., Lu, Y.F., Chen, K.L., Lin, Z.M., 2004. Dating of the Dachang Superlarge tin-polymetallic deposit in Guangxi and its implication for the genesis of the No. 100 Orebody. Acta Geol. Sin. (English Ed.) 78, 452–458.
Wang, D.H., Qin, Y., Wang, C.H., Chen, Y.C., Gao, L., 2012. Mineralization Pedigree for Epithermal Hg, Sb, Au Deposits in Guizhou Province—Taking the Dachang Sb Deposit, the Zimudang Au Deposit and the Luanyantang Hg Deposit for Examples. Geotect. Metall. 36 (3), 330–336 (in Chinese with English abstract).
Wang, G., Hu, R., Su, W., Zhu, L., 2003. Fluid flow and mineralization of Youjiang basin in the Yunnan-Guizhou-Guangxi area, China. Sci. China Earth Sci. 46 (1), 99–109.
Wang, L., Long, C.L., Liu, Y., 2015. Discussion on concealed rock mass delineation and gold source in southwestern Guizhou. Geoscience 29 (3), 703–712 (in Chinese with English abstract).
Wang, L., Zhang, Y.W., Liu, S.G., 2009. The application of regional gravity and magnetic data to delineating intrusive bodies and local geological structures in Guizhou Province. Geophys. Geochim. Explor. 33 (3), 246–249 (in Chinese with English abstract).

Wang, Z.P., Xia, Y., Song, X.Y., Liu, J.Z., Yang, C.F., Yan, B.W., 2013. Study on the evolution of ore-formation fluids for Au-Sb ore deposits and the mechanism of Au-Sb paragenesis and differentiation in the southwestern part of Guizhou Province, China. Chin. J. Geochem. 32 (1), 56–68.

Wilkinson, J.J., 2001. Fluid inclusions in hydrothermal ore deposits. Lithos 55, 229–272.

Williams-Jones, A.E., Norman, C., 1997. Controls of mineral paragenesis in the system Fe-Sb-S-O. Econ. Geol. 92 (3), 308–324.

Wood, S.A., Crerar, D.A., Borcsik, M.P., 1987. Solubility of the assemblage pyrite-pyrrhotite-magnetite-galena-gold-stibnite-bismuthinite-argentite-molybdenite in H_2O-NaCl-CO_2 solutions from 200°C to 350°C. Econ. Geol. 82, 1864–1887.

Xie, Z., Xia, Y., Cline, J.S., Yan, B., Wang, Z., Tan, Q., Wei, D., 2017. Comparison of the native antimony-bearing Paiting gold deposit, Guizhou Province, China, with Carlin-type gold deposits, Nevada, USA. Min. Depos. 52 (1), 69–84.

Xiong, C.J., Liu, J.Z., Liu, S., Wang, D.F., Wang, Z.P., Chen, R., 2013. Study on fluid inclusion of Qinglong Dachang antimony deposit. J. Guizhou Univ. (Nat. Sci. Ed.). 30 (06), 47–52 (in Chinese with English abstract).

Yang, W., Hu, S., Zhang, J.C., Hao, J.L., Lin, Y.T., 2015. NanoSIMS analytical technique and its applications in earth sciences. Sci. China. Earth. Sci. 58 (10), 1758–1767.

Yang, Y.G., Liu, S.R., Jin, Z.S., 2009. Laterization and its control to gold occurrence in Laowanchang gold deposit, Guizhou Province, Southwest of China. J. Geochim. Explor. 100 (1), 67–74.

Ye, Z.J., 1996. The stable isotope and fluid inclusion of the Dachang antimony deposit, Guizhou. Geol. Geochem. 5, 18–20 (in Chinese).

Ye, Z.J., Shi, J.X., Hu, R.Z., 1997. Organic matter and its role in mineralization in Dachang antimony deposit, Guizhou, China. Acta Min. Sin. 17 (03), 310–315 (in Chinese).

Zhang, X.J., Xiao, J.F., 2014. Zircon U-Pb geochronology, Hf isotope and geochemistry study of the Late Permian diabases in the northwest Guangxi autonomous region. Bull. Mineral. Petrol. Geochem. 33, 163–176 (in Chinese with English abstract).

Zhu, J.J., Hu, R.Z., Richards, J.P., Bi, X.W., Stern, R., Lu, G., 2017. No genetic link between Late Cretaceous felsic dikes and Carlin-type Au deposits in the Youjiang basin, Southwest China. Ore Geol. Rev. 84, 328–337.

Zhu, J.J., Zhong, H., Xie, G.Q., Zhao, C.H., Xu, L.L., Lu, G., 2016. Origin and geological implication of the inherited zircon from felsic dikes, Youjiang Basin, China. Acta Petrol. Sin. 32, 3269–3280 (in Chinese with English abstract).

Zhu, Y.N., 2014. Mineralogy and geochemistry of ore minerals in the Woxi Au-Sb-W deposit, western Hunan: Ph.D. thesis, Guiyang, China, Chinese Academy of Sciences (in Chinese with English abstract).

Zhu, Y.N., Peng, J.T., 2015. Infrared microthermometric and noble gas isotope study of fluid inclusions in ore minerals at the Woxi orogenic Au–Sb–W deposit, western Hunan, South China. Ore Geol. Rev. 65, 55–69.